Electronic Supplementary Information to: Standardized microstructure characterization of SOC electrodes as a key element for Digital Materials Design

Philip Marmet,[*a,d] Lorenz Holzer,[a] Thomas Hocker,[a] Gernot K. Boiger,[a] Holger Bausinger,[‡b] Andreas Mai,[§b] Mathias Fingerle,[c] Sarah Reeb,[c] Dominik Michel,[c] and Joseph M. Brader[d]

[a] *Zurich University of Applied Sciences, Institute of Computational Physics, CH-8400 Winterthur, Switzerland. E-mail: mame@zhaw.ch*
[b] *Hexis AG, CH-8404 Winterthur, Switzerland.*
[c] *Math2Market GmbH, D-67657 Kaiserslautern, Germany.*
[d] *Department of Physics, University of Fribourg, CH-1700 Fribourg, Switzerland.*
‡ *Present address: Celeroton AG, CH-8604 Volketswil, Switzerland*
§ *Present address: Topsoe Germany GmbH, Alfredstrasse 81, 45130 Essen , Germany*

Contents

A Introduction to Digital Materials Design (DMD) methods **2**

B Detail settings for the characterization-app **4**
B.1 App options for characterization of different materials and applications 4
B.2 Specification of the used GeoDict modules for the different analysis 5

C Characterization-app option for two-phase electrodes (one solid-phase and one pore-phase) **5**
C.1 Nomenclature for standardized characterization of two-phase electrodes 5
C.1.1 Microstructure characteristics based on 3D image analysis 6
C.1.2 The M-factor for relative diffusivity and single-phase conductivity 8
C.2 Characterization-app GUI-settings for two-phase electrodes (one solid-phase and one pore-phase) 8

D Correlation length fitted to the covariance function **9**

E Computation times for the microstructure characterization **13**

F LSTN-CGO electrodes: materials, fabrication, 3D imaging **14**
F.1 Smart catalyst: properties and powder production of LSTN 14
F.2 Intrinsic MIEC properties of CGO and LSTN: electronic and ionic conductivities 14
F.3 Anode and cell fabrication 15
F.4 3D imaging 15
F.5 Image processing for 3D reconstruction 16

G Details on the LSTN-CGO dataset **18**
G.1 Tomography of the CGO40-LSTN60 sample 18
G.2 Tomography of the CGO60-LSTN40 sample 19
G.3 Tomography of the CGO80-LSTN20 sample 21

H Example for a standardized characterization of virtual three-phase structures from sphere-packing **23**

References **26**

A Introduction to Digital Materials Design (DMD) methods

The introduction of a new materials concept, such as a fully ceramic and composite MIEC electrode, is a challenging task for materials optimization. On the microstructure level, it requires careful adaptation of particle sizes, compositions, porosity and pore size, as well as the reactive surface/interface areas. On the macroscopic level the chemical and thermo-mechanical compatibilities with the neighbouring layers need to be adjusted. To accelerate the research in this field in a cost-efficient way, we suggest to support the development using Digital Materials Design (DMD) methodologies. These methods are especially important for new material-systems, which are not yet well known and need for an efficient screening of suitable concepts. However, the methods are equally applicable for optimization of established material-systems like Ni-YSZ anodes.

In Fig. 1, a DMD workflow for SOC electrodes is suggested. The overall goal of this workflow is to establish a quantitative relationship between fabrication parameters and cell performance, in order to accelerate the microstructure optimization in a systematic and knowledge based way with digital loops. The following sections represent a step-by-step description of this DMD workflow.

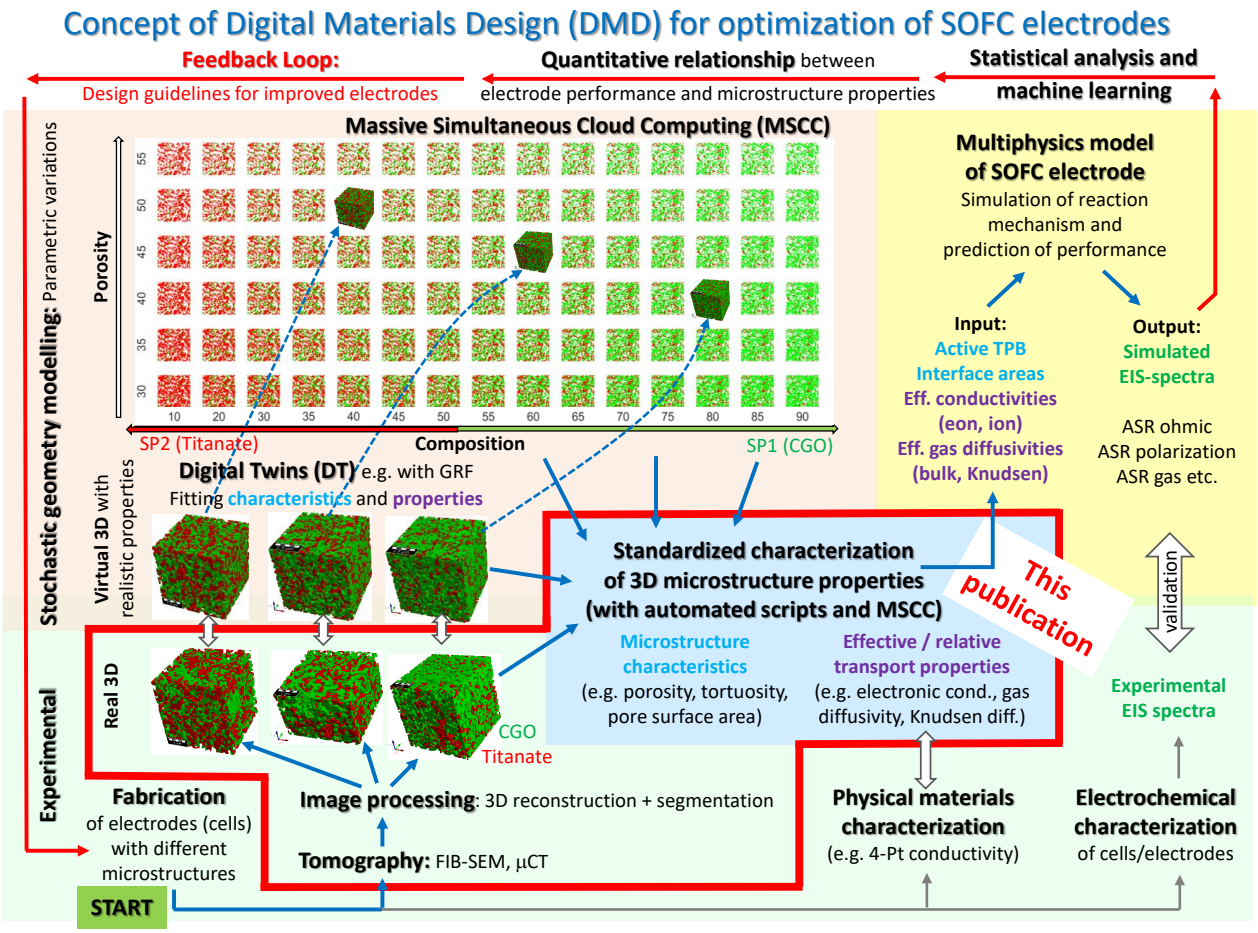

Fig. 1 Overview of workflow and methodologies for Digital Microstructure Design (DMD). The standardized microstructure characterization is highlighted with a red frame.

The basis for the DMD process is a set of fabricated SOC cells. The performances of the cells are experimentally characterized using electrochemical impedance spectroscopy (EIS). In SOFC research, EIS is an essential characterization tool as it allows to distinguish and to quantify different phenomena like e.g., the electrolyte resistance and different physico-chemical processes of the anode and the cathode. Moreover, physical materials characterization is often needed to get the intrinsic properties of the used materials (e.g.,

intrinsic conductivities) or to validate effective properties including microstructure effects (e.g., effective conductivity of the porous electrode). The real microstructures are captured using FIB-SEM tomography for a small number of fabricated cells representing a variation of the parameters, which shall be optimized. For the illustration of the workflow a dataset of three titanate-CGO anodes with different compositions and porosities is used as an example. However, many different optimization parameters could be used as e.g., powder size, sinter temperature etc. Following a procedure of standardized qualitative image processing, the 3D microstructure is reconstructed by filtering and segmentation of the raw data.

The standardized microstructure analysis (highlighted with a red frame in Fig. 1) described in the main article is a key element of this DMD workflow. Microstructure analysis of the real structures from tomography (and subsequently also for virtual structures) enables to quantify all relevant morphological characteristics (tortuosity, constrictivity, TPB as well as surface and interface areas). Furthermore, virtual testing by 3D numerical simulation is used to characterize the associated effective or relative transport properties. This comprehensive set of microstructure properties can be used for a direct comparison of the important microstructure effects for the realized structures. Moreover, the microstructure properties can be used as input for a multiphysics model. This model is then capable to predict the cell performance for different microstructure scenarios.

Stochastic modeling is then used for parametric studies where microstructure properties are varied systematically. Numerous virtual 3D microstructures can be realized efficiently with stochastic modeling. However, the stochastic model also needs to be fitted to realistic microstructures from laboratory experiments. For this purpose, stochastic digital microstructure twins (i.e., microstructure descriptions based on stochastic geometry) with matching microstructure properties are then constructed for each real structure (i.e., for each dataset from FIB-SEM tomography). In the current example, the virtual structures are constructed with an approach that is based on pluri-gaussian random fields[1,2]. The phase volume fractions, specific interface areas, three-phase boundary lengths and effective transport properties of the virtual structures are matched to real structures from FIB-SEM tomography in order to obtain the digital microstructure twins. Thereby, the standardized microstructure analysis is a key element in order to compare the relevant microstructure properties of the real and virtual structures. Alternative structure generators based on sphere-packing algorithms are also available, especially for electrodes for which the original grains from the powder are still present in the porous structure. However, for sintered materials such as the SOC electrodes, these conventional structure generators turned out to be of limited use. On that basis (i.e., with a stochastic model based on a pluri-Gaussian method and fitted to real 3D structures from FIB-SEM), the microstructure can be varied for a large parameter space in a realistic way. In the current example, the composition (i.e., relative phase volume fractions of titanate and CGO) and the porosity are varied. The full set of microstructure properties is determined for the virtual structures using the standardized microstructure characterization.

A multiscale-multiphysics simulation model is then used to predict the impact of the microstructure variation on the electrode performance (i.e., area specific resistance ASR_{tot}). The model needs to reflect all the relevant physico-chemical processes involved like the transport of charge carriers in the solid phases, transport of the gas species in the pore-phase and the reaction kinetics. The microstructure properties of the virtual structures obtained by the standardized microstructure characterization are thereby the most relevant input. In addition, the model needs to be calibrated to the experimental performance characterization of the cells (e.g., EIS results). Especially the parameters for the reaction kinetics (e.g., exchange current density) usually needs to be fitted to the experimental data. This model-based performance prediction enables to establish the relationship between fabrication parameters, microstructure properties and cell-performance. On this basis, design guidelines for the fabrication of improved electrode performance can be provided, which closes the loop of this iterative workflow. This feedback-loop can be supported by statistical analysis and machine learning techniques using the data within the specific study and might even be complemented with additional information from similar available studies (e.g., data from public repositories and literature).

This DMD process presented for the example of titanate-CGO SOFC-anodes can of course also be used for other SOC electrodes with different materials. More general, this DMD process is also applicable for other energy materials as e.g., for batteries. However, some modules of the process can be applied directly, while others need to be adapted to the specific system studied.

B Detail settings for the characterization-app

B.1 App options for characterization of different materials and applications

The characterization-app can be applied for all common SOC electrodes and for different study goals. In Fig. 2, some example settings are provided for three-phase electrodes (two solid phases and one pore-phase).

		Checkboxes																	Fields										
		Contiguous / discontiguous phase analysis	Use maximum parallelization	Delete large intermediate data	Solid-phase characterization	Simulation of conductivities	Interface resistance	Morphological analysis of the solid phases	Morphological analysis of the original solid phases	Morphological analysis of the contiguous solid phases	Compute correlation functions	Pore-phase characterization	Compute bulk diffusion	Compute Knudsen diffusion	Compute permeability	Compute percolation tortuosity	Morphological analysis of the original pore-phase	Morphological analysis of the contiguous pore-phase	Structure name	# of boundary voxels to crop	Process parallelization (number of cores)	Characterization direction	Number of solid phases	Pairs of intrinsic solid-phase conductivities	List of interface resistances	Material of SP1 solid-phase 1 (SP1)	Material of SP2 solid-phase 2 (SP2)	Max. length scale for correlation functions	Number of samplings for the correlation functions	Length of in- and outflow zone in voxels
Case	**Characterization**	1	2	3	4	5	6	7	8	9	10	11	12	13	14	15	16	17	1	2	3	4	5	6	7	8	9	10	11	12
Ni-YSZ	Basic	☑	☐	☑	☑	☑	☐	☐	☐	☐	☐	☑	☑	☑	☑	☐	☐	☐	Name.gdt	0	4	Z	2	[[1,0],[0,1]]	-	YSZ	Ni	175	500'000	100
	Extended	☑	☐	☐	☑	☑	☐	☑	☐	☑	☑	☑	☑	☑	☑	☐	☐	☑	Name.gdt	0	4	Z	2	[[1,0],[0,1],[1,1]]	-	YSZ	Ni	175	500'000	100
Ni-CGO	Basic	☑	☐	☑	☑	☑	☐	☐	☐	☐	☐	☑	☑	☑	☑	☐	☐	☐	Name.gdt	0	4	Z	2	[[1,0],[0.0001,1]]	-	CGO	Ni	175	500'000	100
	Extended	☑	☐	☐	☑	☑	☐	☑	☐	☑	☑	☑	☑	☑	☑	☐	☐	☑	Name.gdt	0	4	Z	2	[[1,0],[0,1],[1,1],[0.0001,1]]	-	CGO	Ni	175	500'000	100
LST-CGO	Basic	☑	☐	☑	☑	☑	☐	☐	☐	☐	☐	☑	☑	☑	☑	☐	☐	☐	Name.gdt	0	4	Z	2	[[0.1,1],[1,0.1]]	-	CGO	LST	175	500'000	100
	Extended	☑	☐	☐	☑	☑	☐	☑	☐	☑	☑	☑	☑	☑	☑	☐	☐	☑	Name.gdt	0	4	Z	2	[[1,0],[0,1],[1,1],[0.1,1],[1,0.1]]	-	CGO	LST	175	500'000	100
SP1-SP2	Only pore-phase, Kn ≥1	☑	☐	☐	☐	☐	☐	☐	☐	☐	☐	☑	☑	☑	☑	☐	☐	☑	Name.gdt	0	4	Z	2	-	-	-	-	-	-	100
	Only pore-phase, Kn <<1	☑	☐	☐	☐	☐	☐	☐	☐	☐	☐	☑	☑	☐	☐	☐	☐	☑	Name.gdt	0	4	Z	2	-	-	-	-	-	-	-
	Only solid phases	☑	☐	☐	☑	☑	☐	☑	☐	☑	☑	☐	☐	☐	☐	☐	☐	☐	Name.gdt	0	4	Z	2	[[1,0],[0,1],[1,1],[0.1,1],[1,0.1]]	-	SP1	SP2	175	500'000	-
	Minimal & fast	☑	☐	☐	☑	☐	☐	☐	☐	☐	☐	☐	☐	☐	☐	☐	☐	☐	Name.gdt	0	4	Z	2	-	-	SP1	SP2	175	500'000	-

Fig. 2 Setting examples for the characterization-app for common cases. Typical settings are presented for three-phase electrodes for a structure size of NXxNYxNZ = 400x350x500 voxels. The checkboxes and fields correspond to the GUI reported in Fig. 8 of the main article. Colour groups: grey = general settings, light red = solid-phase analysis, light blue = general pore-phase analysis and dark blue = pore-phase analysis relevant for large Knudsen numbers $Kn \gtrsim 1$ (i.e., nano-porous structures).

The 'basic' characterization settings are the minimal settings to determine all the relevant microstructure parameters, which can for example be used as an input for the parametrization of a multiphysics electrode model. For the 'extended' setting, additional morphological characteristic and additional conductivity reference cases are determined, which allow for a detailed study of the microstructure features relevant for the empirical microstructure optimization. The checkboxes and fields (see also GUI in Fig. 8 of the main article) are summarized in different colour groups: grey = general settings, light red = solid-phase analysis, light blue = general pore-phase analysis and dark blue = pore-phase analysis relevant for large Knudsen numbers $Kn \gtrsim 1$ (i.e., nano-porous structures). The parameters in the fields 10, 11 and 12 are chosen for a structure size of NXxNYxNZ = 400x350x500 voxels. The maximal allowed value for field 10 is min(NX,NY,NZ)/2= 350/2=175. The number of voxels for field 12 should be around 20 % of the structure size in the computation direction (i.e., Z in our example) and thus 100 voxels.

Different cases for composite material systems are reported, which corresponds to typical SOFC anodes: Ni-YSZ, Ni-CGO and LST-CGO. Note that the recommended checkbox selections are identical for these three examples. Moreover, only the field 6 with the "pairs of intrinsic solid-phase conductivities" vary conceptionally. For Ni-YSZ, the single-phase conductivities are relevant (i.e., [1,0] and [0,1]) and the relative conductivity of SP tot ([1,1]) might be a useful reference case for the extended characterization. For Ni-CGO, the relative ionic single-phase conductivity of CGO ([1,0]) and the relative electronic composite conductivity ([0.0001,1]) are the important measures, while the single-phase conductivity of Ni ([0,1]) and of SP tot ([1,1]) might be useful reference cases for the extended characterization. For LST-CGO, the relative ionic ([1,0.1]) and the relative electronic ([0.1,1]) composite conductivity are the important measures, while the single-phase conductivity of CGO ([1,0]), the single-phase conductivity of LST ([0,1]) and of SP tot ([1,1]) might be useful reference cases for the extended characterization. Note that the meaning of the parameter

names sigma_eff_Case1-sigma_eff_Case5 for the relative conductivities in the tables 9 and 11 of the main article are not unique but do change according to the definition of field 6.

Moreover, some further frequently used settings are reported for a general three-phase composite material with SP1-SP2. Two different settings are suggested for studies, where only the microstructure properties of the pore-phase are of interest, depending on the pore-size. Note that for nano-porous structures with a Knudsen number of $Kn \gtrsim 1$ the diffusivity is strongly reduced by the Knudsen effect. The combined bulk and Knudsen diffusion can for example be described appropriately with the dusty-gas model, which needs the relative Knudsen diffusivity $D^{\text{sim}}_{\text{Kn,rel}}$, the characteristic Knudsen length $d_{\text{Kn,pore}}$ and the gas permeability κ^{sim} as additional inputs to the bulk diffusivity. However, the two needed simulations for these properties are computational quite costly. Thus, it is worth checking if they are really needed for a specific study. In addition, also the settings for an 'extended' characterization of only the solid phases are reported. Furthermore, the "minimal & fast" settings include all the characterizations, which can be calculated in a comparably short time. With these settings, the phase volume fractions, the volume specific interface areas and TPB-length are reported for the contiguous and the original phases. These settings are useful for a first fast overview of the microstructure properties. Moreover, this analysis might for example be sufficient for a porous catalyst layer (not for SOC applications), where no transport is involved within the microstructure.

It must be emphasized that the suggested setting examples do by no means aim for completeness and they can be adapted according to the actual goals of a specific study.

B.2 Specification of the used GeoDict modules for the different analysis

The characterization-app is a Python based script, which can be executed in the GeoDict[3] software package and uses different GeoDict modules. A list of the GeoDict modules used for the different microstructure analysis is reported in table 1.

Table 1 Specification of the used GeoDict modules for the different microstructure analysis in the characterization-app. The referenced tables can be found in the main article.

Analysis	Results	GeoDict module
Contiguous/discontiguous phase analysis	Contiguous / discontiguous geometry features	Porodict / Open and Closed Porosity
Phase volume fractions	Properties of table 1 (e.g., ε, ϕ_{SP1}, ϕ_{SP2} etc.)	Porodict / Open and Closed Porosity
Interface properties	Volume specific interface areas and TPB-length (table 2)	MatDict / Estimate Surface Area and Estimate Three-Phase Contact Line
Continuous-phase size distributions (c-PSD) and MIP phase size distributions (MIP-PSD)	Mean radius of bulges r_{max} and bottlenecks r_{min} and constrictivity β (tables 3, 4 and 5)	Compute Tortuosity app or PoroDict / Pore Size Distribution (Granulometry and Porosimetry)
Covariance function	Covariance function $C_X(h)$ and correlation length l_{corr} for SP1, SP2 and pore-phase (section 2.2.6 of the main article)	MatDict and general GeoDict functionalities
Tortuosity analysis	Direct geometric (table 6), mixed physics-based / geometric (table 7) and indirect physics-based (table 8) tortusities	Compute Tortuosity app
Prediction of the M-factors with morphological characteristics	Predicted relative diffusivity and conductivity (table 10, e.g., $D^{\text{pred,I}}_{\text{rel}}$, $\sigma^{\text{predI}}_{\text{rel}}$ etc.)	Compute Tortuosity app including various underlying solvers and modules
Prediction of the gas permeability	Predicted hydraulic radii r_{hcI}, r_{hcII} and predicted permeabilities κ^{predI}, κ^{predII} (table 12)	Compute Tortuosity app
Gas diffusivity analysis	Relative gas diffusivity simulated $D^{\text{sim}}_{\text{rel}}$ (table 9)	Compute Tortuosity app / DiffuDict, LIR solver
Conductivity analysis	Simulated relative single-phase conductivities $\sigma^{\text{sim}}_{\text{rel}}$ (table 9) and relative electronic $\sigma^{\text{sim}}_{\text{rel,eon,comp}}$ and ionic $\sigma^{\text{sim}}_{\text{rel,ion,comp}}$ composite conductivity (table 11).	ConductoDict, EJ solver
Knudsen diffusion analysis	Knudsen relative diffusivity simulated $D^{\text{sim}}_{\text{Kn,rel}}$, Knudsen characteristic length $d_{\text{Kn,pore}}$ (table 13)	Compute Tortuosity app / DiffuDict, random walk method
Permeability analysis	Gas permeability simulated κ^{sim} (table 12)	FlowDict, Stokes (LIR) solver

C Characterization-app option for two-phase electrodes (one solid-phase and one pore-phase)

C.1 Nomenclature for standardized characterization of two-phase electrodes

Commonly, three-phase material systems (two solid-phases and a pore-phase) are used for SOC electrodes. However, MIEC electrodes can also consist of only one solid phase. Moreover, current collector layers often consist of only one porous material. Such two-phase structures (i.e., one pore- and one solid-phase) can also be analysed with our characterization-app by choosing the appropriate option. For two-phase structures, the

number of needed microstructure properties is substantially reduced. In section C.1.1, the used variables and parameter names used in the characterization-app are documented in order to provide a consistent nomenclature for two-phase structures. The microstructure characteristics for the pore-phase remain unchanged but are reported once again for completeness. The additional pore-phase characterization for the parametrization of the dusty-gas model are reported in section 2.3.3 of the main article and are not repeated here. The appropriate GUI-settings of the characterization-app for two-phase electrodes are reported in section C.2. Note that this app-options for two-phase electrodes can also be used for the characterization of general porous media applications.

C.1.1 Microstructure characteristics based on 3D image analysis

C.1.1.1 Contiguous phase analysis

In porous structures, there is the possibility that there are trapped pores, which do not contribute to the gas transport and the fuel oxidation reaction. For two-phase systems with one solid and one pore phase, solid islands surrounded by air are non-physical and can be considered as artefacts. In this case, the contiguity analysis for the solid phase can be used to remove these artefacts. The corresponding variables and parameter names are listed and described in table. 2.

Table 2 Variable and parameter definition and description associated with volume fractions. The discontiguous volume fraction are the differences between original volume fractions and contiguous volume fractions and do not have a separate parameter name. Abbreviations: cont=contiguous and discont = discontiguous.

Porosity	ε	Epsilon	-
Porosity, contiguous portion	$\varepsilon_{\mathrm{cont}}$	Epsilon_cont	-
Porosity, discontiguous portion (i.e., trapped pores)	$\varepsilon_{\mathrm{discont}}$	-	-
Solid volume fraction	ϕ	SVF	-
Solid volume fraction, contiguous portion	ϕ_{cont}	SVF_cont	-
Solid volume fraction SP1, discontiguous portion	ϕ_{discont}	-	-

C.1.1.2 Volume specific surface area

For two-phase systems, the interface properties reduce to one interface, which can be described as volume specific pore surface area. The contiguity analysis allows to distinguish between the contiguous surface portion accessible for the gas species and the discontiguous surface portions (trapped pores), which is inactive. The corresponding variables and parameter names are listed and described in table 3.

Table 3 Variable and parameter definition and description associated with interface areas two-phase structures. The discontiguous values are the differences between the values considering the original volume fractions and contiguous volume fractions and do not have a separate parameter name in the characterization-app. Abbreviations: cont=contiguous and discont = discontiguous.

Description	Variable	Parameter	Unit
Volume specific surface area of pores	$S_{\mathrm{V,pore}}$	S_V_pore	$\mu\mathrm{m}^{-1}$
Volume specific surface area of pores, contiguous	$S_{\mathrm{V,pore,cont}}$	S_V_pore_cont	$\mu\mathrm{m}^{-1}$
Volume specific surface area of pores, discontiguous (trapped pores)	$S_{\mathrm{V,pore,discont}}$	-	$\mu\mathrm{m}^{-1}$

C.1.1.3 Contiguous phase size distributions (c-PSD/Granulometry) with $r_{\max}$ and MIP phase size distribution (MIP-PSD/Porosimetry) with $r_{\min}$ for two-phase structures

The parameters for the size distributions are analogous to the three-phase structures but with only one solid phase to be characterized. The corresponding variables and parameter names are listed and described in table 4 and 5.

Table 4 Variable and parameter definition for the continuous-phase size distribution (c-PSD). Abbreviations: cont = contiguous.

Description	Variable	Parameter	Unit
Mean radius of bulges of the contiguous solid-phase	$r_{\mathrm{max,SP,cont}}$	r_max_SP_cont	µm
Mean radius of bulges of the contiguous pore-phase	$r_{\mathrm{max,pore,cont}}$	r_max_pore_cont	µm

Table 5 Variable and parameter definition for the MIP phase size distribution. Abbreviations: cont = contiguous.

Description	Variable	Parameter	Unit
Mean radius of bottlenecks of the contiguous solid-phase	$r_{\mathrm{min,SP,cont}}$	r_min_SP_cont	µm
Mean radius of bottlenecks of the contiguous pore-phase	$r_{\mathrm{min,pore,cont}}$	r_min_pore_cont	µm

The corresponding constrictivity variables and parameters are reported in table 6

Table 6 Variable and parameter definition and description associated with the constrictivity. Abbreviations: cont = contiguous.

Description	Variable	Parameter	Unit
Constrictivity of the contiguous solid-phase	$\beta_{\mathrm{SP,cont}} = \left(\frac{r_{\mathrm{min,SP,cont}}}{r_{\mathrm{max,SP,cont}}}\right)$ (1)	Beta_SP_cont	-
Constrictivity of the contiguous pore-phase	$\beta_{\mathrm{pore,cont}} = \left(\frac{r_{\mathrm{min,pore,cont}}}{r_{\mathrm{max,pore,cont}}}\right)$ (2)	Beta_pore_cont	-

C.1.1.4 Tortuosity analysis

There are many different concepts to determine tortuosities and a few of them are reported within our standard characterization. A comprehensive discussion about different types of tortuosities can be found in the book of Holzer et al.[4]. In this section, the tortuosities relevant for two-phase structures are reported. Following the nomenclature of Holzer et al.[4], the tortuosities can be classified according to their method of determination and to their type of definition. For the group class A, the method of determination is direct (i.e., directly from the geometry) and the type of definition is geometric. A representative of this class is the geodesic tortuosity $\tau_{\mathrm{dir,geod}}$ which is determined with GeoDict on the contiguous phases. The corresponding variables are reported in table 7.

Table 7 List of selected tortuosity types belonging to class A: direct, geometric tortuosities. Abbreviations: dir = direct, geod = geodesic and cont = contiguous.

Description	Variable	Parameter	Unit
Geodesic tortuosity of the contiguous solid-phase	$\tau_{\mathrm{dir,geod,SP,cont}}$	Tau_dir_geodesic_SP_cont	-
Geodesic tortuosity of the contiguous pore-phase	$\tau_{\mathrm{dir,geod,pore,cont}}$	Tau_dir_geodesic_pore_cont	-

For the group class B, the method of determination is mixed (i.e., path-length based on volume fields of numerical transport simulation) and the type of definition is mixed as well (i.e., mix of geometric and physical definition). The corresponding variables are reported in table 8 for the physics of charge transport $\tau_{\mathrm{mixed,ele,Vav}}$, diffusion $\tau_{\mathrm{mixed,diff,Vav}}$ and gas-flow $\tau_{\mathrm{mixed,hydr,Vav}}$.

Table 8 List of selected tortuosity types belonging to class B: mixed types with both, physics-based and geometric definitions. Abbreviations: ele = electric, Vav = volume averaged, diff = diffusion and hydr = hydraulic.

Description	Variable	Parameter	Unit
Volume averaged tortuosity from current density field, solid-phase	$\tau_{\mathrm{mixed,ele,Vav}}$	Tau_mixed_ele_Vav	-
Volume averaged tortuosity from diffusionflux field, pore-phase	$\tau_{\mathrm{mixed,diff,Vav,pore}}$	Tau_mixed_diff_Vav	-
Volume averaged tortuosity from flowfield, pore-phase	$\tau_{\mathrm{mixed,hydr,Vav}}$	Tau_mixed_hydr_Vav	-

For the group class C, the method of determination is indirect (i.e., no path-length measurement) and the type of definition is physics based. The corresponding variables are reported in table 9 for the physics of charge transport $\tau_{\mathrm{indir,ele}}$, bulk diffusion $\tau_{\mathrm{indir,diff}}$, Knudsen diffusion $\tau_{\mathrm{indir,Kn}}$ and gas-flow $\tau_{\mathrm{indir,hydr\,I}}$ / $\tau_{\mathrm{indir,hydr\,II}}$.

Table 9 List of selected tortuosity types belonging to class C: indirect / physics-based tortuosities. Abbreviations: ele = electric, indir = indirect, cont = contiguous, diff = diffusion, hydr = hydraulic and Kn = Knudsen.

Description	Variable	Parameter	Unit
Indirect conduction tortuosity, solid-phase	$\tau_{\mathrm{indir,ele}}$	Tau_indir_ele	-
Indirect diffusive tortuosity, pore-phase	$\tau_{\mathrm{indir,diff,pore}}$	Tau_indir_diff	-
Indirect hydraulic tortuosity I, pore-phase	$\tau_{\mathrm{indir,hydr\,I,cont}}$	Tau_indir_hydr_I_cont	-
Indirect hydraulic tortuosity II, pore-phase, pore-phase	$\tau_{\mathrm{indir,hydr\,II,cont}}$	Tau_indir_hydr_II_cont	-
Knudsen tortuosity X-direction, pore-phase	$\tau_{\mathrm{indir,Kn,X}}$	Tau_indir_Kn_X	-
Knudsen tortuosity Y-direction, pore-phase	$\tau_{\mathrm{indir,Kn,Y}}$	Tau_indir_Kn_Y	-
Knudsen tortuosity Z-direction, pore-phase	$\tau_{\mathrm{indir,Kn,Z}}$	Tau_indir_Kn_Z	-

C.1.2 The M-factor for relative diffusivity and single-phase conductivity

The parameters for the simulated M-factors are summarized in table 10.

Table 10 Variable and parameter definition associated with the M-factor simulation (with Laplace equation) for the relative conductivity and diffusivity. Abbreviations: rel = relative and sim = simulated.

Description	Variable	Parameter	Unit
Relative gas diffusivity, simulated	$D_{\mathrm{rel}}^{\mathrm{sim}}$	D_rel_sim	-
Relative single-phase conductivity of the solid-phase, simulated	$\sigma_{\mathrm{rel}}^{\mathrm{sim}}$	sigma_rel	-

The M-factor predictions for the relative conductivity and diffusivity for the solid- and the pore-phase are summarized in table 11.

Table 11 Description of predicted relative transport properties (equivalent to M^{pred}) with the corresponding expressions and nomenclature of parameters, for conduction and diffusion. Abbreviations: pred = predicted, cont = contiguous, dir = direct and geod = geodesic.

Description	Expression		Parameter	Unit
Relative conductivity pred. I of the contiguous solid-phase	$\sigma_{\mathrm{rel}}^{\mathrm{pred\,I}} = \frac{{\phi_{\mathrm{cont}}}^{1.15}{\beta_{\mathrm{SP,cont}}}^{0.37}}{{\tau_{\mathrm{dir,geod,SP,cont}}}^{4.39}}$	(3)	sigma_rel_I_pred_cont	-
Relative conductivity pred. II of the contiguous solid-phase	$\sigma_{\mathrm{rel}}^{\mathrm{pred\,II}} = \frac{{\phi_{\mathrm{cont}}}^{1.67-0.48\beta_{\mathrm{SP,cont}}}}{{\tau_{\mathrm{dir,geod,SP,cont}}}^{5.18}}$	(4)	sigma_rel_II_pred_cont	-
Relative gas diffusivity pred. I of the contiguous pore-phase	$D_{\mathrm{rel}}^{\mathrm{pred,I}} = \frac{{\varepsilon_{\mathrm{cont}}}^{1.15}{\beta_{\mathrm{pore,cont}}}^{0.37}}{\tau_{\mathrm{dir,geod,pore,cont}}^{4.39}}$	(5)	D_rel_I_pred_cont	-
Relative gas diffusivity pred. II of the contiguous pore-phase	$D_{\mathrm{rel}}^{\mathrm{pred\,II}} = \frac{{\phi_{\mathrm{pore,cont}}}^{1.67-0.48\beta_{\mathrm{pore,cont}}}}{{\tau_{\mathrm{dir,geod,pore,cont}}}^{5.18}}$	(6)	D_rel_II_pred_cont	-

C.2 Characterization-app GUI-settings for two-phase electrodes (one solid-phase and one pore-phase)

The characterization-app also includes an option for the characterization of porous layers with only one solid phase. Possible examples are pure CGO-anodes[5–8] or current collection layers of pure Ni or perovskite[8]. Many of the parameters are identical for the case of three phases reported in section 2.4 of the main article. Thus, in this section only the parameters are discussed which are different.

If the field 5 is changed from 2 to 1, the GUI reported in Fig. 8 of the main article changes to the GUI displayed in Fig. 3. Checkbox 18 enables the numerical computation of the relative conductivity of the solid phase. In field 13, the name of the material can be specified. In checkbox 19, the morphological analysis as

described in section 2.2 of the main article can be enabled. Checkbox 20 enables the morphological analysis of the original structure and checkbox 21 the morphological analysis of the contiguous structure after the contiguity analysis. In general, the latter option is sufficient.

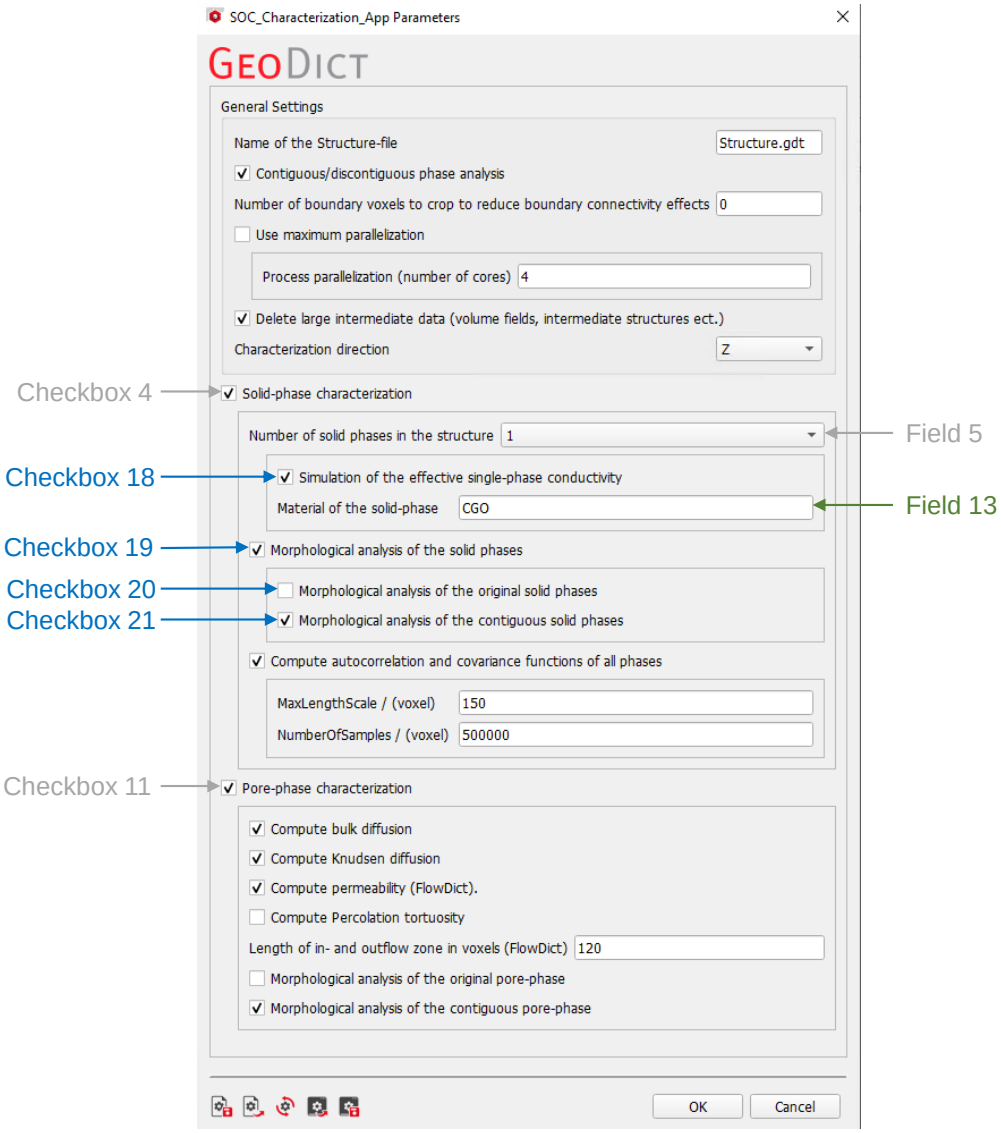

Fig. 3 App for the standardized and automated microstructure characterization for SOC electrodes in GeoDict: Options for the characterization of one solid-phase electrodes. Many of the parameters are identical to the case of three phases reported in section 2.4 of the main article. Thus, only the parameters are indicated, which are different (except of the grey coloured labels, which are repeated).

Note that this app-options for two-phase electrodes can also be used for the characterization of general porous media applications. If only the pore-phase is of interest, the checkbox 4 (solid-phase characterization) can be disabled.

D Correlation length fitted to the covariance function

The correlation length l_{corr} of the covariance function provides a measure for the spatial distribution and thus the characteristic phase size. Moreover, the correlation length is also a fundamental parameter for the virtual reconstruction for example based on Gaussian random fields. In this contribution, two different approaches to estimate the correlation length are provided. For fit 1, a Gauss function is directly fitted to the autocorrelation function (the relation between the autocorrelation function and the covariance function is

provided in Eq. 8). For fit 2, the covariance function is fitted to an analytical covariance function based on a Gaussian model. In order to match the surface area according to Eq. 8 of the main article, only the first zone of the covariance function in the range of the correlation length is used for the fit 2. Further details about the fitting of the correlation length is reported below in this section.

To estimate the correlation length according to fit 1, a Gauss-function is fitted to the autocorrelation function:

$$f_{\text{Gauss}}(h) = \exp\left(\frac{-h^2}{2 \cdot l^2_{\text{corr, fit1}}}\right) \tag{7}$$

where $l_{\text{corr, fit1}}$ is used as an estimate for the correlation length. Note that the autocorrelation function $R_X(h)$ is directly linked to the covariance function $C_X(h)$ as follows:

$$C_X(h) = R_X(h) \cdot \sigma_X^2 + \mu_X^2 \tag{8}$$

where the mean value $\mu_X = \phi_X$ corresponds to the phase volume fraction and σ_X is the standard deviation of all voxel values, which are either 0 or 1. The autocorrelation function is computed with GeoDict[3] and the covariance function is then deduced with Eq. 8 in our characterization-app.

For fit 2, the covariance function is fitted to an analytical covariance function based on a Gaussian model. The two-point covariance function $C_X(h)$ of a binary phase-pair (e.g., 0 for the pore-phase and 1 for the solid phase) can be calculated from the correlation function of a random field $\rho_X(h)$[2]:

$$C_X(h) = \frac{1}{2\pi} \int_1^{\rho_X(h)} \frac{1}{\sqrt{1-r^2}} \exp\left(\frac{-\lambda_X^2}{1+r}\right) dr + \varepsilon_X \tag{9}$$

where ε_X is the phase volume fraction, λ_X is the threshold for the standard normal cumulative distribution function in order to obtain the defined volume fraction ε_X. In order to estimate the correlation length l_{corr} of the covariance function $C_X(h)$ a Gaussian model is used for $\rho_X(h)$:

$$\rho_{\text{fit2}}(h) = \exp\left(\frac{-h^2}{2 \cdot l^2_{\text{corr, fit2}}}\right) \tag{10}$$

To obtain a good estimate for the correlation length, $l_{\text{corr, fit2}}$ is fitted in a iterative procedure. On the basis of a starting value of $l_{\text{corr, fit2}}$, the covariance function for the Gauss-model is computed and the mean squared error is determined and minimized with a simple iterative procedure using a correction for $l_{\text{corr, fit2}}$ in every iteration. For cases, where the covariance function of a structure cannot be fully described by a Gaussian model, especially the slope at h=0 (which corresponds to the volume specific surface area) is not well captured if the whole range of the covariance function is used. Moreover, too high correlation lengths result, which would e.g., correspond to an overestimation of the bulge-radii. If only the first few data points are used covering approximately the correlation length, the slope is captured much better. Even if the mean squared error is larger, the main features are captured better, while the other features can simply not be captured by a Gaussian model.

For illustration, the covariance functions and the corresponding correlation length are determined for three synthetic microstructures with different phase volume fractions reported in Fig. 4 a)-c). The structures are generated by thresholding a Gaussian random field, which is defined by a Gaussian correlation function identical to the used fit function of Eq. 10 with a defined correlation length of $l_{\text{corr}} = 0.2\,\mu$m. The corresponding calculated covariance functions for the three structures are plotted in Fig. 4 d) together with the analytical functions with fitted correlation length. As the structures are based on a Gaussian random field, the fit is very good. In Fig. 4 e) the corresponding fitted correlation length are plotted for the different fits. The defined correlation length is plotted as a dashed line. Fit 2 is fitted only on the first part corresponding to the correlation length and fit 3 is fitted to the whole range of the correlation function. For this ideal case, the differences for the correlation length for fit 2 and fit 3 are marginal and are very close to the defined correlation length. Note that the defined and fitted correlation lengths do not vary for the different volume fractions. For fit 1, where the covariance function is fitted directly to a Gauss-function (not using Eq. 9), the correlation lengths are systematically lower about 25 % and do also vary for the different volume fractions.

For a better guess, the correlation length fitted by fit 1 might be scaled by about a factor of 1.33.

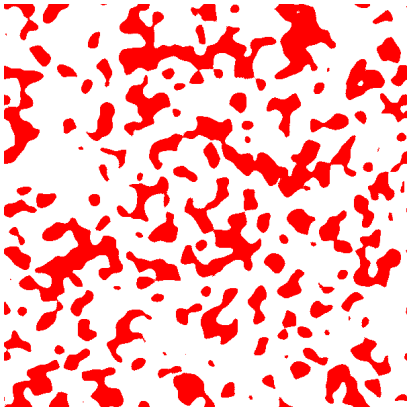

(a) GRF-structure, $\phi = 30\,\%$.

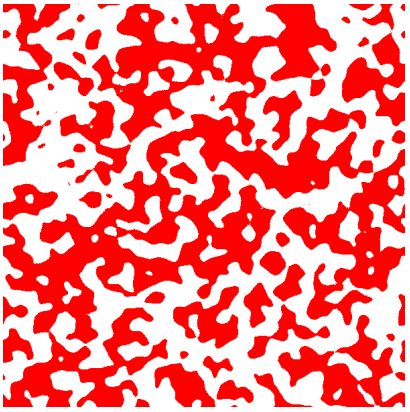

(b) GRF-structure, $\phi = 50\,\%$.

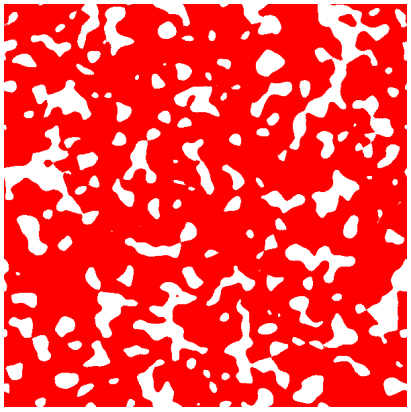

(c) GRF-structure, $\phi = 75\,\%$.

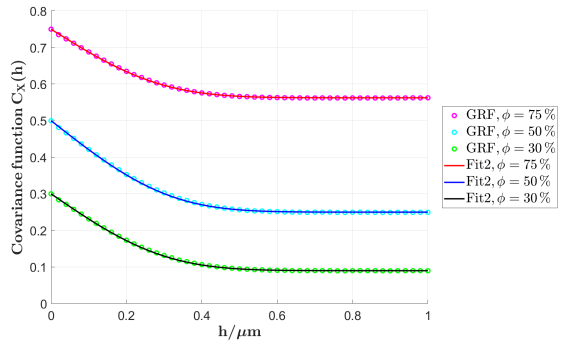

(d) Covariance functions.

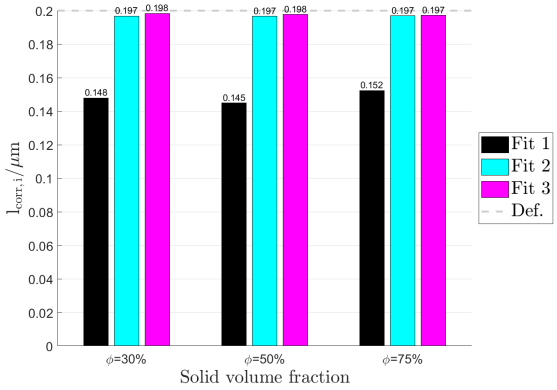

(e) Correlation length.

Fig. 4 Test structures generated by thresholding a Gaussian random field with different solid phase volume fractions: a)-c) 2D orthoslices of the 3D structures d) computed and fitted analytical covariance functions, e) correlation length with fit 1, fit 2 and fit 3.

In Fig. 5, the covariance functions of the LSTN-CGO dataset are approximated with the fit 2 and fit 3. The corresponding fits of the correlation lengths are reported in Fig. 6 b) and c). For the structure CGO40-LSTN60, where the fits with the Gaussian model match quite well, the correlation lengths with fit 2 and fit 3 are quite close. For cases where the Gaussian model does not fit well, the differences for the correlation length with fit 2 and fit 3 are quite large (up to a factor of two).

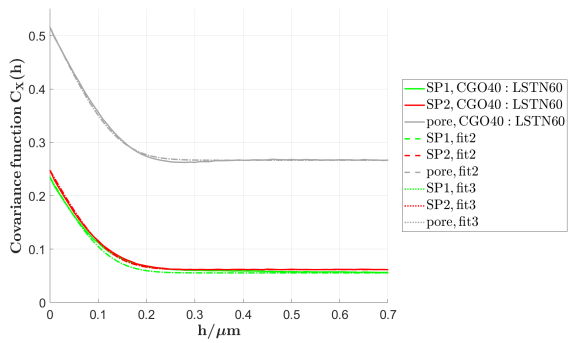

(a) CGO40-LSTN60.

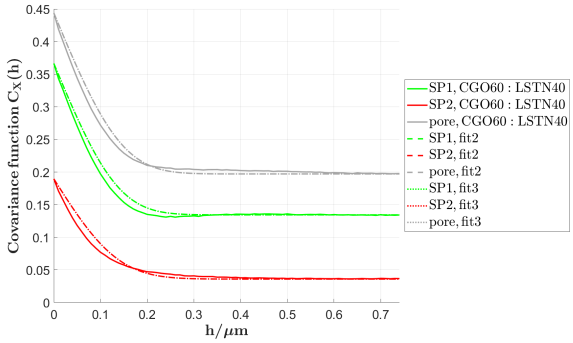

(b) CGO60-LSTN40.

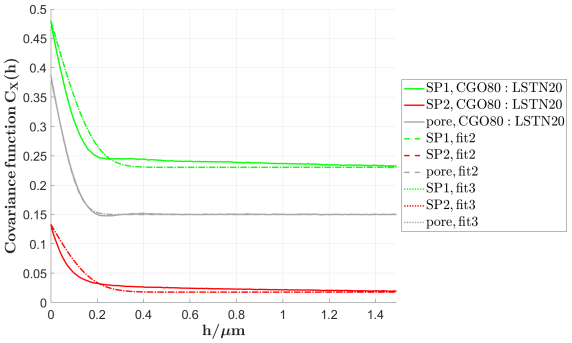

(c) CGO80-LSTN20.

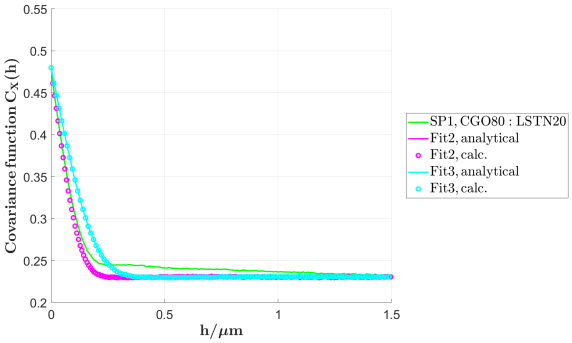

(d) LSTN20-CGO80, verification for SP1 (CGO).

Fig. 5 Fit of the covariance functions with fit 2 and fit 3 for the CGO-phase (SP1), the LSTN-phase (SP2) and the pore-phase for the LSTN-CGO dataset: a) CGO40-LSTN60, b) CGO60-LSTN40, c) CGO80-LSTN20 and d) comparison of the analytical covariance functions to those computed for virtual structures generated with Gaussian random fields for SP1 (CGO) of the CGO80-LSTN20 structure and for fit 2 and fit 3.

The meaning of the different fits (i.e., fit 2 and fit 3) shall be illustrated by constructing the corresponding GRF-structure for SP1 of the CGO20-LSTN80 structure (the corresponding procedure will be described in detail in a separate publication of this series). The computed correlation functions with fit 2 and fit 3 for the realized structures are reported in Fig. 5 d), showing a very good agreement to the analytical functions. Three selected microstructure properties for the two structures are compared to the original tomography in table 12. The total volume specific interface area and the radii of the bulges and bottlenecks are much better matched with fit 2. Thus, the correlation length of fit 2 is a better estimate to describe the structure than the correlation length of fit 3, even if it owns the larger mean square error for the fit.

Table 12 Comparison of the total volume specific interface area $IA_{V,SP}$ and the mean radius of the bulges $r_{max,SP}$ and bottlenecks $r_{min,SP}$ for the solid phase SP1 (CGO) from tomography and from a Gaussian random field (GRF) reconstruction with fit 2 (fit to match the total volume specific interface area) and fit 3 (fit over the whole range).

Description	Variable	Unit	Tomography	GRF Fit 2	GRF Fit 3
Total volume specific interface area of SP1	$IA_{V,SP}$	μm^{-1}	8.21	8.25	5.55
Mean radius of bulges of the solid phase	$r_{max,SP}$	μm	0.094	0.090	0.134
Mean radius of bottlenecks of the solid phase	$r_{min,SP}$	μm	0.073	0.070	0.104

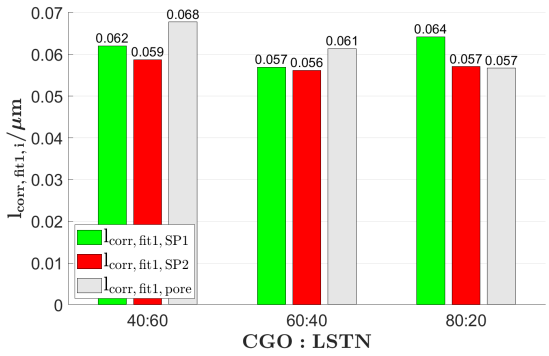

(a) Correlation length fit 1: fitted Gauss function.

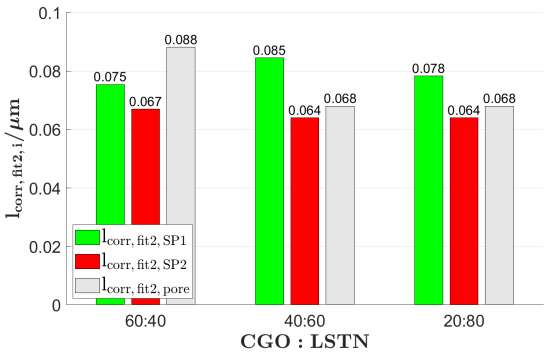

(b) Correlation length fit 2: fitted covariance function with Gauss model, tuned to match the surface area.

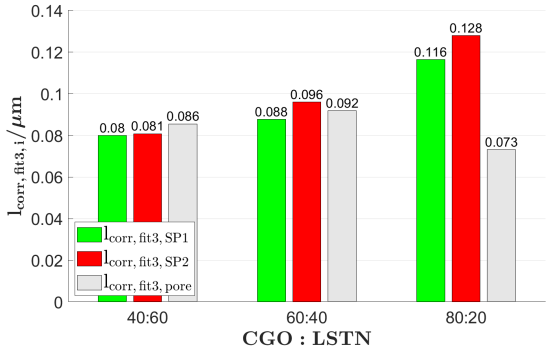

(c) Correlation length fit 3: fit of the covariance function over the whole range.

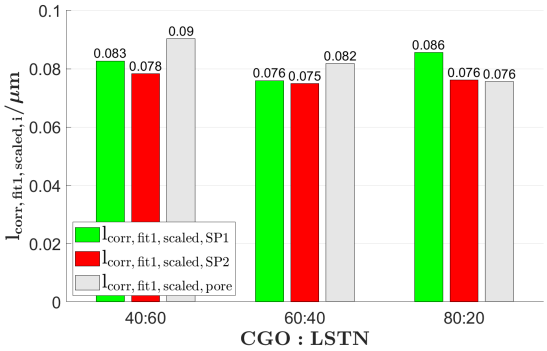

(d) Correlation length fit 1 scaled: fitted Gauss function with correction.

Fig. 6 Fitting of the correlation length of the CGO-phase (SP1) for the CGO80-LSTN20 structure: a) fit 1: fitted Gauss function to the autocorrelation function, b) fit 2: fitted covariance function with Gauss model, tuned to match the surface area, c) fit 3: fit of the covariance function over the whole range and d) fit 1 scaled: fitted Gauss function with correction.

For fit 1, where the correlation function is directly fitted to a Gauss function, the values for the correlation length (Fig. 6 a)) are closer to fit 2 (Fig. 6 b)) than to fit 3 (Fig. 6 c)), but are systematically underestimated as already observed for the GRF test structures in Fig. 4 c). Using a correction factor of 1.33 as estimated above, the correlation length corresponds significantly better with fit 2, as reported in Fig. 6 d). Thus, the simple fit procedure with fit 1 might be a suitable approximation for the correlation length, if a correction factor is used.

E Computation times for the microstructure characterization

The computation times for the full standard characterization (with similar app settings shown in Fig. 8 of the main article) of the different sample structures are reported in table 13. The characterizations were performed on a common workstation and 4 processors were used for the calculation. The computation times strongly depend on the structure sizes (i.e., number of voxels to compute), which are reported as well. The needed structure size for a representative elementary volume (REV) depends on the structure type and voxel resolution. It also varies for different properties (e.g., for volume fractions and interface areas the REV is much smaller than for tortuosity and constrictivity). In this context it must be mentioned that the image volume of our tomography structures is probably too small to reach REV for all properties. The computation time thereby rises more than proportional to the structure sizes (3D image volume), which can be observed for the reported computation times per million voxels. The computation time can be lowered by reducing the number of characterized microstructure properties, if not all of them are needed. For example, the reported times in table 13 also include the morphological parameters for the original phase volume fractions and not only for the contiguous phases, which is normally not necessary. Several typical study settings are

suggested in section B.1. Another way to reduce the computation time is to use Massive Simultaneous Cloud Computing (MSCC) for the parallel computation. This is particularly important for the analysis of a large number of structures (e.g., from stochastic microstructure modeling results).

Table 13 Computation times for the full standard characterization of the different structures discussed in this contribution.

Case	Structure size NXxNYxNZ / vox	Computation time / h	Comp. time per Mio voxel / h / Mio vox
Tomography CGO40-LSTN60	300x384x384 = $44 \cdot 10^6$	1.1	0.025
Tomography CGO60-LSTN40	384x384x157 = $23 \cdot 10^6$	0.6	0.026
Tomography CGO80-LSTN20	384x384x384 = $56 \cdot 10^6$	1.5	0.026
Sphere-packing sample A (SP1:SP2:pore=30:20:50)	600x600x600 = $216 \cdot 10^6$	12.5	0.058
Sphere-packing sample B (SP1:SP2:pore=40:30:30)	600x600x600 = $216 \cdot 10^6$	8.1	0.038
Sphere-packing sample C (SP1:SP2:pore=40:40:20)	600x600x600 = $216 \cdot 10^6$	7.6	0.035

F LSTN-CGO electrodes: materials, fabrication, 3D imaging

The possibilities of the characterization-app to perform quantitative microstructure analysis is illustrated in the results part of the main article. For this illustration we use a series of 3D microstructures from real and virtual SOFC anodes as input to the characterization-app. In the following section, we are focusing on the first illustration example, i.e., on the real anodes consisting of CGO and LSTN (more precisely: (La,Sr)(Ti,Ni)O3-perovskite). The materials properties, the fabrication of powders and electrodes, and the methods of 3D imaging and 3D reconstruction are briefly described.

F.1 Smart catalyst: properties and powder production of LSTN

The LSTN material used for these anodes has quite unique properties. In addition to the MIEC properties, this titanate also provides "smart catalyst" properties based on Ni-nanoparticles that are hosted on the titanite surface. Under normal circumstances, Ni-nanoparticles tend to lose their catalytic properties relatively quickly due to coking, sulphur poisoning and agglomeration. In the new LSTN material, the Ni-nanoparticles can be regenerated by redox-cycling. Under oxidating conditions, (i.e., when the fuel is switched off), the oxidation process leads to an uptake of Ni-ions into the crystal lattice of the perovskite. Under reducing anode conditions (i.e., when fuel is switched on), the Ni-ions are driven out from the crystal lattice, so that new Ni-nanoparticles are formed on the LSTN surface. Redox cycling is thus not harmful to this catalyst, as it is for normal Ni-containing anodes, but it rather has a revitalizing effect. Thereby, nickel remains distributed in fine particles and retains its catalytic function even when operated with sulphur-containing fuels. The LSTN material was developed in an SNF-project (NRP70, Energy Turnaround) and further information can be found here[9].

The synthesis of the LSTN perovskite is based on a modified citrate-gel technique, which is described in Burnat et al.[10]. The stoichiometric formula of the LSTN-perovskite is $La_xSr_{1-1.5x}Ti_{1-y}Ni_yO_{3-\delta}$. The maximum amount of Ni that can be incorporated upon calcination at 650°C (under oxidizing conditions) on the B-site (replacing Ti) is 5 atom % (i.e., y max = 0.05). Optimal properties in terms of the initial powder properties (such as single-phase purity, phase stability) and anode material properties (e.g., functionality of smart catalyst as well as MIEC and electrical conductivities) were found for the following A-site deficient composition: $La_{0.3}Sr_{0.55}Ti_{0.95}Ni_{0.05}O_{3-\delta}$. Note that an A-site deficiency can enhance the electronic and ionic conductivity of LST-perovskites[11]. LSTN powders with this perovskite composition (abbreviated in[10] as LST35.5-5Ni) were then used for fabrication of LSTN-CGO anodes and subsequent performance tests with EIS. The microstructures of these composite anodes are also investigated in the present study.

F.2 Intrinsic MIEC properties of CGO and LSTN: electronic and ionic conductivities

The intrinsic conductivities of the two electrode materials are estimated from available experimental and literature data as reported in table 14. For CGO10 (i.e., Ce-oxide with 10 % doping of Gd), relatively precise conductivity data are available[12]. However, for LSTN the experimental results are less precise so that only the order of magnitude can be estimated[13,14]. Based on the available data, it is justified to make the

simplified assumption that LSTN has a factor of 10 higher intrinsic electronic conductivity and a factor of 10 lower intrinsic ionic conductivity compared to CGO. Hence, in a MIEC anode consisting of LSTN and CGO, both phases will contribute to the transport of both charge carriers. This so-called composite conductivity is an important advantage of MIEC anodes, compared to anodes consisting of single-phase conductors. Nevertheless, due to the different intrinsic conductivities the average current density for electrons will be much higher in the LSTN-phase and for ions the average current density will be higher in the CGO-phase. These phenomena will be illustrated and discussed based on the results from the characterization-app.

Table 14 List for the estimated intrinsic conductivities of CGO and LSTN at a temperature of $T = 850°C$. For the ionic conductivity of CGO a reference oxygen partial pressure of $p_{O2} = 3 \cdot 10^{-20}$ bar was used, which corresponds to hydrogen with a water content of 7 %.

Material	Intrinsic electronic conductivity	Intrinsic ionic conductivity	Reference
CGO	$\sigma_{0,\mathrm{eon,CGO}} = 1.83\,\mathrm{S/cm}$	$\sigma_{0,\mathrm{ion,CGO}} = 0.13\,\mathrm{S/cm}$	[12]
LSTN	$\sigma_{0,\mathrm{eon,LSTN}} = 18.3\,\mathrm{S/cm}$	$\sigma_{0,\mathrm{ion,LSTN}} = 0.013\,\mathrm{S/cm}$	[13,14]

F.3 Anode and cell fabrication

In this study, we use microstructure data from LSTN-CGO anodes with three different phase compositions (i.e., varying the CGO/LSTN-ratio). The entire fabrication process of such titanate-CGO anodes was described in a previous publication[13]. Button cells for EIS-testing and subsequent 3D microstructure characterization are produced by screen-printing of electrode pastes on a commercial solid electrolyte from Kerafol (scandium-stabilized Zr-oxide). Materials and processes for paste production, screen printing, sintering, and EIS-measurements follow the descriptions given in Burnat et al.[13]. For our study, the pastes compositions were adapted so that the nominal anode compositions reveal CGO/LSTN-ratios of 40:60, 60:40, and 80:20 (by solid volume %).

F.4 3D imaging

3D-microstructures of the three MIEC anodes are investigated with FIB-SEM tomography (see reviews of FIB-tomography Uchic et al.[15], Holzer and Cantoni[16], Cantoni and Holzer[17]). After EIS-characterization, the button cell samples are impregnated with a low viscosity resin (4 parts Araldite BY158 mixed with 1 part Aradur hardener, supplied by Huntsman). The embedded samples are then cut into small pieces of ca. 5-10 mm edge lengths, by using a diamond saw (and/or with TXP Leica). The sample surfaces are treated by grinding, polishing and finally coating with a thin carbon layer. Mechanical polishing is performed on textile substrates with diamond suspensions of 6 µm, 3 µm and 1 µm (MetaDi mono-crystalline diamond suspension, Buehler). The samples are then glued on an Al-stub using silver paste. For conductive coating (ca. 10 nm thick carbon layers) we used an SCD50 from Bal-Tec.

FIB-SEM-tomography is performed with a Helios Nanolab 600i (DualBeam FIB from FEI), located at the Scientific Center for Optics and Microscopy at ETH Zürich (ScopeM, https://scopem.ethz.ch). Acquisition of image stacks by FIB tomography includes the following steps: a) Gas assisted metal deposition of a 1 µm thick Pt- or C-layer in order to protect the surface from ion milling artefacts. b) Preparation of a cube with suitable dimensions (10 to 20 µm edge lengths) in order to reduce shadowing effects and re-deposition. c) Automated acquisition of an image stack is obtained by repeated and alternating execution of erosion (i.e., FIB milling with a gallium liquid metal ion source (Ga LMIS) and 2D imaging (with SEM). This serial sectioning procedure, which is also called 'slice and view', was done with an ion beam current of 0.77 nA and an accelerating voltage of 30 kV. SEM imaging was performed using the so-called through-the-lens detector (TLD) at 2.0 kV accelerating voltage, 0.34 nA beam current and 30 µs dwell time. The magnification for SEM-image acquisition and the step size for FIB-slicing was chosen in such way that the resulting voxel resolution is 10 nm in x-, y-, and z-directions. The acquired raw data from FIB-SEM tomography then consisted of stacks with 500 to 1'000 sequential SEM images.

F.5 Image processing for 3D reconstruction

Reconstruction of the 3D anode microstructure based on raw data from FIB-SEM tomography was done with GeoDict software. All necessary image processing options dedicated for filtering and reconstruction of FIB-SEM stacks are implemented in this software. For 3D reconstruction of LSTN-CGO anodes, we used the following image processing steps:

a) Variations in the average grey scale of single images can be removed with the flickering filter. These variations in slicing direction (z) are usually caused by instabilities of the SEM detectors.

b) After removal of the flickering, the images of the stack are repositioned relative to each other, in order to compensate for mechanical and electromagnetic drifts in x- and y-directions. For this purpose, a stack alignment option is available.

c) Another artefact from FIB serial sectioning is the so-called curtaining effect. Due to local variations in the FIB-milling efficiency, the exposed imaging plane can reveal unwanted ripples. These ripples are then seen as vertical stripes in the SEM images. This artefact, also called waterfall effect, can be removed with a dedicated curtaining filter. For larger stacks, this correction procedure may take several hours.

d) The stack of 2D images can now be considered as a 3D image volume. The dimensions of the voxels, i.e., 3-dimensional picture elements) are now identical to the pixel dimensions of the SEM images (in x- and y-directions) and the FIB-slicing step size in z-direction (i.e., effective distance between the single images). In some cases, it is necessary to apply a so-called resampling procedure, in order to transform the resolution of the image data into isometric voxels. In our case, this is done in such way that the resulting voxels are 10 nm in each direction.

e) Depending on the imaging conditions (e.g., beam current, contrast-brightness-settings, scanning rate/dwell time, detector type and sensitivity), the acquired SEM images may be more or less noisy. There are numerous noise filters available (e.g., median or gauss filters). For our purpose, we use the NLM-filter (non-local means), since this algorithm maintains sharp edges at phase interfaces, while smoothing noise within the phase domains. This filtering procedure may also take up to three hours, depending on image volume and NLM settings.

f) From the filtered and realigned stack, a suitable region of interest is then cropped, so that the image volume contains homogeneous and representative microstructure information.

g) In the grey-scale image volume, the pore-phase appears as dark (black), LSTN as bright (white) and CGO as intermediate (grey) phase. When the image quality is high (i.e., high contrast, low noise), the three phases can easily be segmented with a simple thresholding step. For three-phase materials like LSTN-CGO anodes, a multiple-threshold option must be chosen for segmentation of all three phases.

h) Due to imaging imperfections (i.e., limited resolution, large excitation volume), there are always some voxels with intermediate grey scale values at the interface between the brightest (LSTN) and the darkest phase (pores). Due to the thresholding procedure, these voxels are erroneously attributed to the intermediate phase (CGO). Hence, thresholding always results in apparent CGO-rim artefacts at the interface between LSTN and pore. This artificial CGO rim are removed with the so-called cleanse option, which is actually a modification of the morphological opening process. It includes a dilation step of the pore-phase at the expense of CGO, followed by a dilation step of LSTN at the expense of the pores. In this way, the CGO rims are removed, but otherwise the initial grain structure and phase identification from threshold segmentation is maintained.

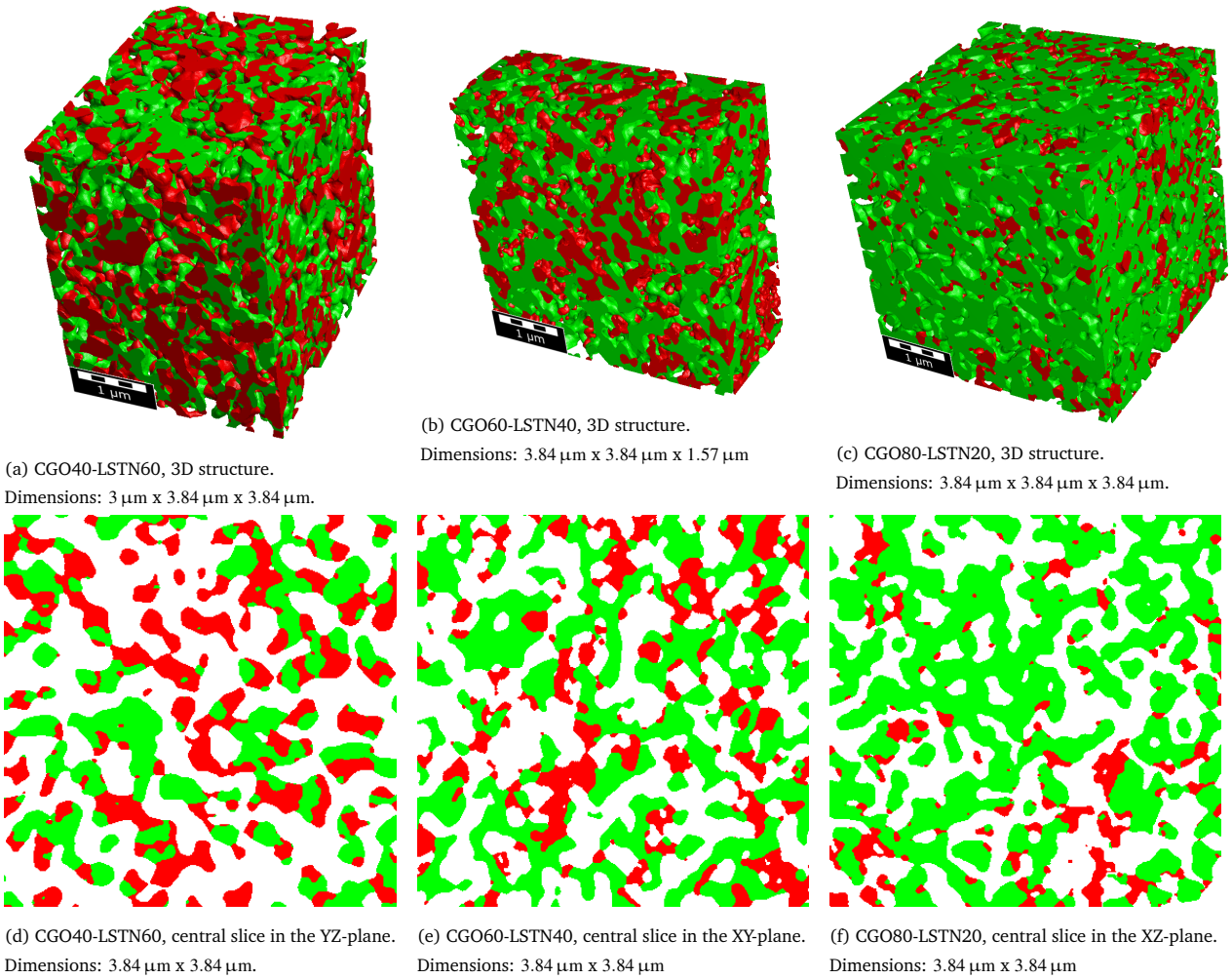

(a) CGO40-LSTN60, 3D structure.
Dimensions: 3 µm x 3.84 µm x 3.84 µm.

(b) CGO60-LSTN40, 3D structure.
Dimensions: 3.84 µm x 3.84 µm x 1.57 µm

(c) CGO80-LSTN20, 3D structure.
Dimensions: 3.84 µm x 3.84 µm x 3.84 µm.

(d) CGO40-LSTN60, central slice in the YZ-plane.
Dimensions: 3.84 µm x 3.84 µm.

(e) CGO60-LSTN40, central slice in the XY-plane.
Dimensions: 3.84 µm x 3.84 µm

(f) CGO80-LSTN20, central slice in the XZ-plane.
Dimensions: 3.84 µm x 3.84 µm

Fig. 7 3D-view and central orthoslices of the tomography structure for CGO40-LSTN60 a)/d), CGO60-LSTN40 b)/e) and CGO80-LSTN20 c)/f). Colour code: green = CGO, red = LSTN, white/transparent = pore.

The resulting 3D microstructures from FIB-SEM imaging, after filtering, alignment and segmentation, are visualized in Fig. 7 (also reported in the main article as Fig. 9). The three-phase structures consist of pore-phase (white) and CGO (green, also called solid phase SP1) and LSTN (red, SP2). The nominal (target) composition for the first structure (Fig. 7 a) and d)) is CGO:LSTN=40:60 (solid vol.%), which is not very well matched by the effective (measured) composition (i.e., CGO:LSTN=49:51). The original structure that was reconstructed from tomography had a cube-size of 384^3 voxels (see ESI section G.1, Fig. 8). However, significant CGO-agglomeration was observed at some locations within the microstructure (also documented in the ESI section G.1 – see Figs. 8 a) and c)). For simplification, in the present study this heterogeneous region was removed by cropping. The resulting cube has a size of 300x384x384 voxels, as shown in Figs. 7 a) and d) (additional orthoslices are shown in Fig. 9 in the ESI section G.1). The nominal composition for the second structure is CGO:LSTN=60:40 (solid vol.%). The original structure with a size of 384x384x256 voxels (see Fig. 10 in the ESI section G.2) is affected by an artificial horizontal shift within the structure (ESI section G.2, Fig. 10 a)). In order to remove this artefact, also this structure is cropped to a size of 384x384x157 voxels, which is shown in Figs. 7 b) and e). Note that the volume of this structure might be smaller than the REV, which will be considered in the results discussion. The nominal composition for the third structure (Figs. 7 c) and f)) is CGO:LSTN=80:20 (solid vol.%) and the full tomography structure with a cube-size of 384^3 voxels is used. Also this sample shows some inhomogeneities due to CGO-agglomeration, which will be accounted for in the results discussion. (Additional orthoslices are shown in Fig. 12 in the ESI section G.3).

G Details on the LSTN-CGO dataset

G.1 Tomography of the CGO40-LSTN60 sample

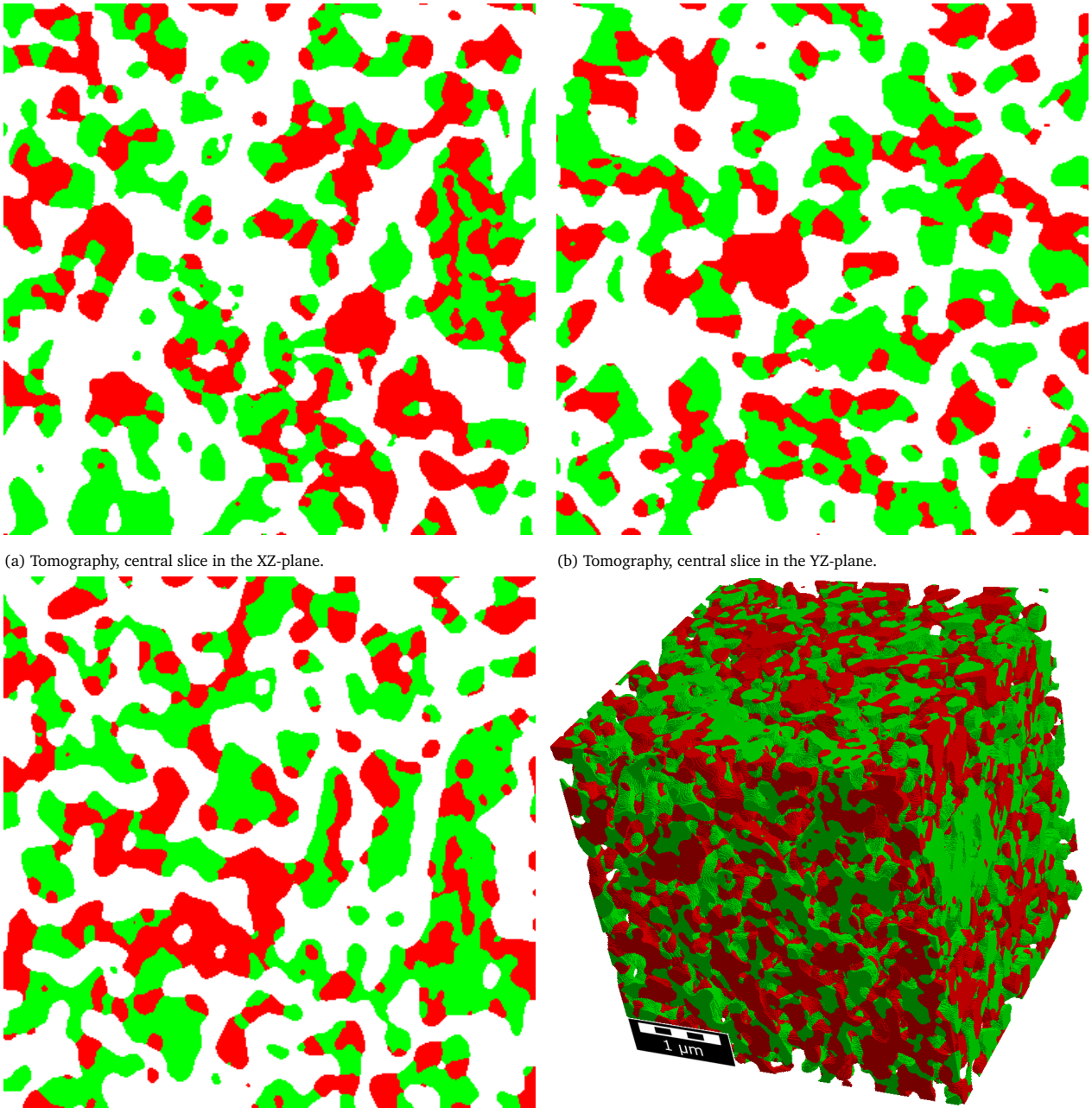

(a) Tomography, central slice in the XZ-plane.

(b) Tomography, central slice in the YZ-plane.

(c) Tomography, central slice in the XY-plane.

(d) Tomography, 3D structure.

Fig. 8 Original CGO40-LSTN60 tomography structure: central orthoslices a)-c) and 3D-view d). Colour code: green = CGO, red = LSTN, white/transparent = pore. The sample volume is a cube with a side length of 3.84 µm.

In this section the original and the cropped CGO40-LSTN60 tomography structures are reported in more detail. The original tomography structure is reported in Fig. 8 and is a three-phase structure with one pore-phase (white) and two solid-phases LSTN (red) and CGO (green). The nominal composition is CGO:LSTN=40:60 which is not very well matched by the effective composition CGO:LSTN=49:51 of the characterized sample volume. The structure has a cube-size of 384^3 voxels. However, there is a CGO-agglomeration visible on the right side of the orthoslices in the XZ-plane (Fig. 8 a)) and the XY-plane (Fig. 8 c)). This agglomeration cannot be captured with the current virtual structures and is also not representa-

tive concerning the size of the image-window. Therefore, this region is cropped and a reduced region with 300x384x384 voxel is used as reported in Fig. 9. This cropped structure is also used for the determination of the microstructure properties described in section 3.1.1 of the main article. A selection of microstructure properties for this cropped structure is also reported in table 14 in the main article.

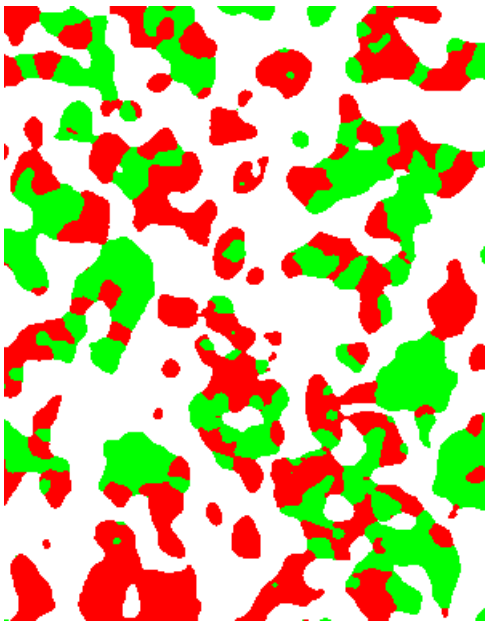

(a) Tomography, central slice in the XZ-plane.

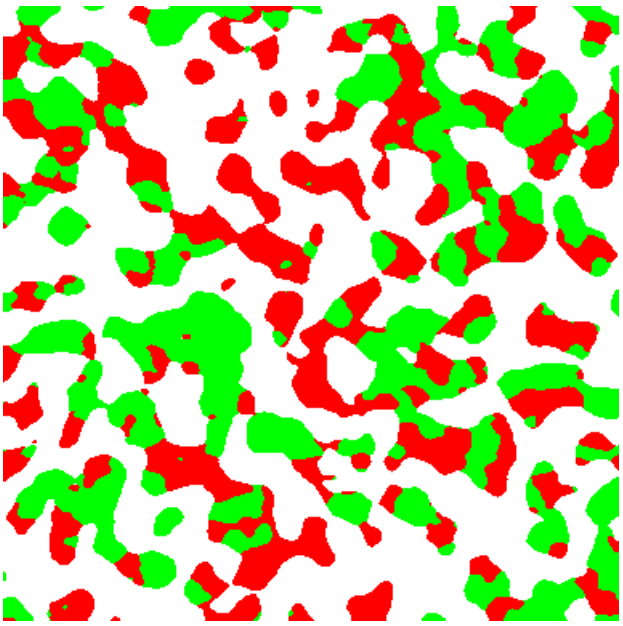

(b) Tomography, central slice in the YZ-plane.

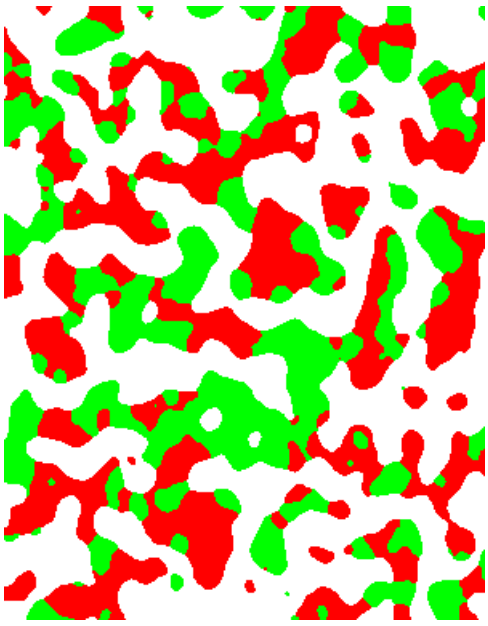

(c) Tomography, central slice in the XY-plane.

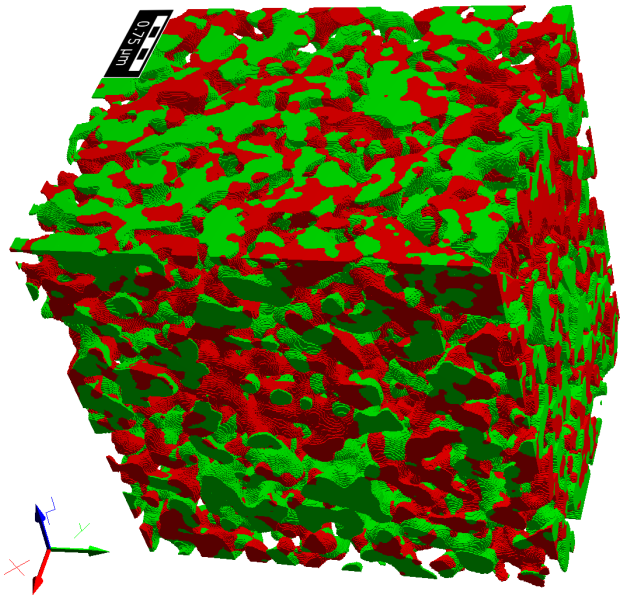

(d) Tomography, 3D structure.

Fig. 9 Cropped CGO40-LSTN60 tomography structure: central orthoslices a)-c) and 3D-view d). Colour code: green = CGO, red = LSTN, white/transparent = pore. The cropped structure has the dimensions 3 µm x 3.84 µm x 3.84 µm

G.2 Tomography of the CGO60-LSTN40 sample

In this section the original and the cropped CGO60-LSTN40 tomography structures are reported in more detail. The original tomography structure is reported in Fig. 10 and is a three-phase structure with one pore-phase (white) and two solid-phases LSTN (red) and CGO (green). The nominal composition is CGO:LSTN=60:40 which is not very well matched by the effective composition CGO:LSTN=66:34 of the

characterized sample volume. The structure has a size of 384x384x256 voxels. As visible in Fig. 10 a), there is an artificial horizontal shift within the structure, which seriously disturbs the microstructure properties. Therefore, the structure used for the microstructure characterization is cropped to a size of 384x384x157 voxels, as reported in Fig. 11. Note that this structure might be to small to be considered as a representative elementary volume (REV), which needs to be considered for the discussion of the data. This cropped structure is also used for the determination of the microstructure properties described in section 3.1.1 of the main article. A selection of microstructure properties for this cropped structure is also reported in table 14 in the main article.

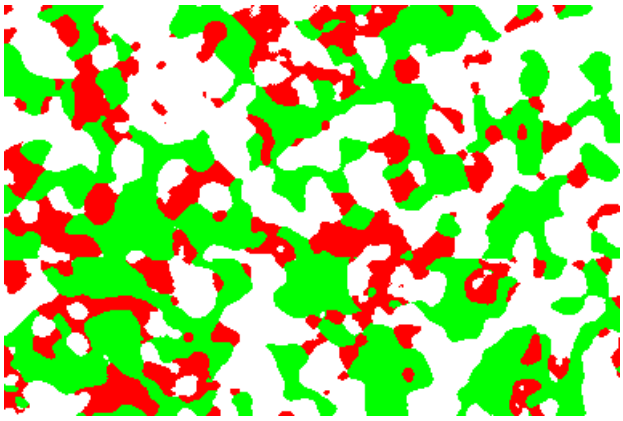

(a) Tomography, central slice in the XZ-plane.

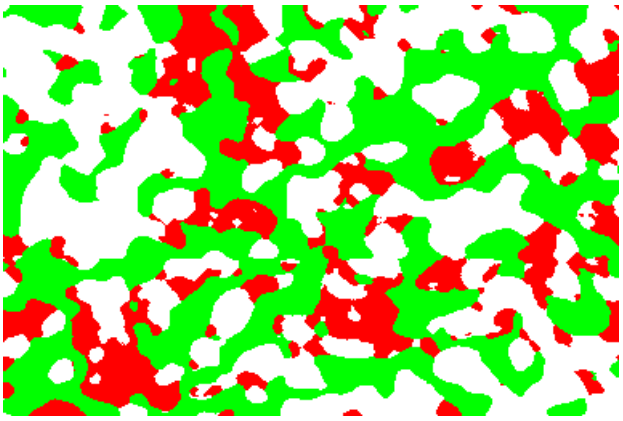

(b) Tomography, central slice in the YZ-plane.

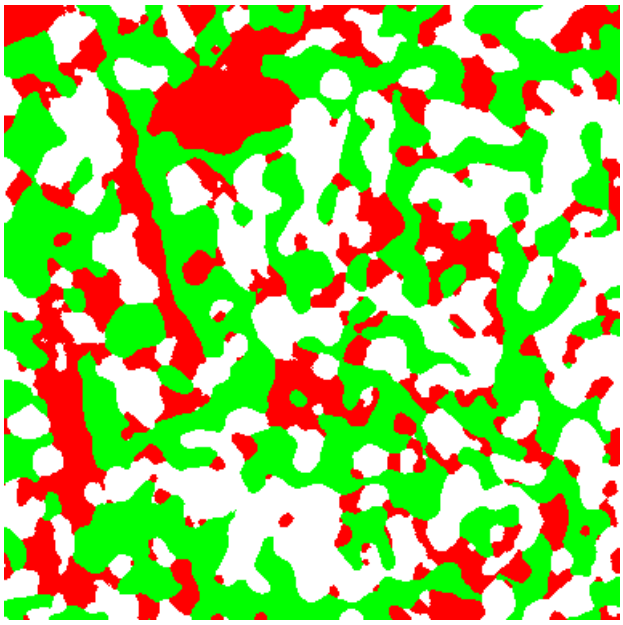

(c) Tomography, central slice in the XY-plane.

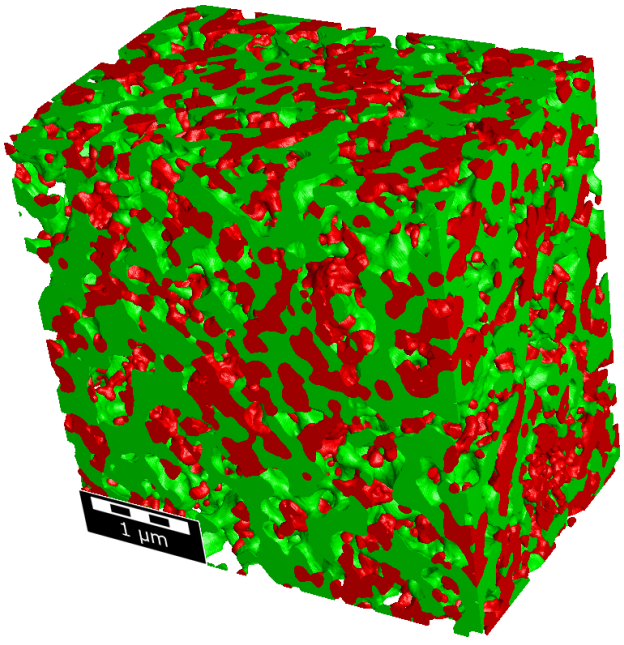

(d) Tomography, 3D structure.

Fig. 10 Original CGO60-LSTN40 tomography structure: central orthoslices a)-c) and 3D-view d). Colour code: green = CGO, red = LSTN, white/transparent = pore. 3.84 µm x 3.84 µm x 2.56 µm.

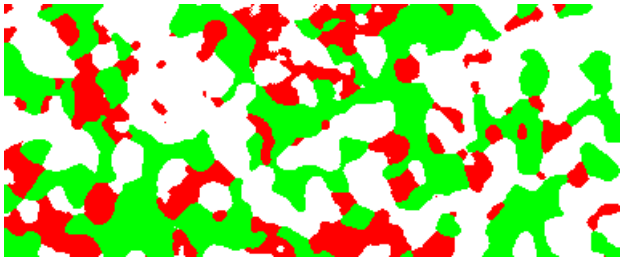

(a) Tomography, central slice in the XZ-plane.

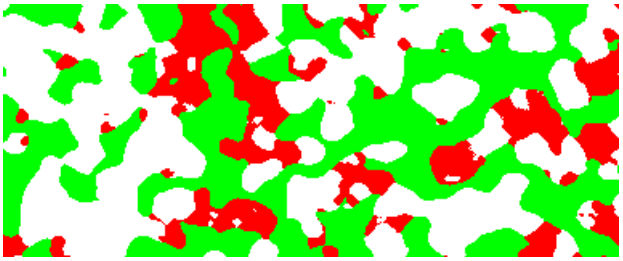

(b) Tomography, central slice in the YZ-plane.

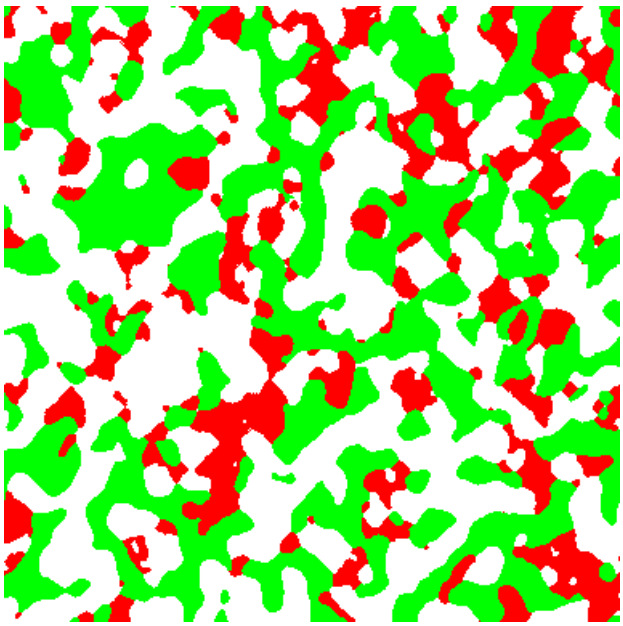

(c) Tomography, central slice in the XY-plane.

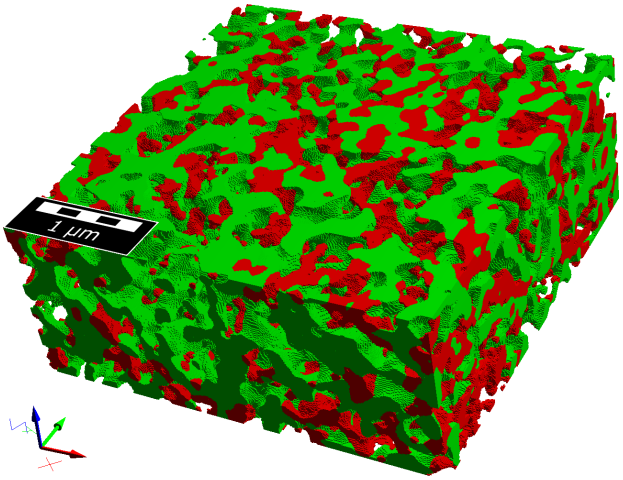

(d) Tomography, 3D structure.

Fig. 11 Cropped CGO60-LSTN40 tomography structure: central orthoslices a)-c) and 3D-view d). Colour code: green = CGO, red = LSTN, white/transparent = pore. The cropped structure has the dimensions 3.84 µm x 3.84 µm x 1.57 µm

G.3 Tomography of the CGO80-LSTN20 sample

In this section the CGO80-LSTN20 tomography structure is reported in more detail. The original tomography structure is reported in Fig. 12 and is a three-phase structure with one pore-phase (white) and two solid-phases LSTN (red) and CGO (green). The nominal composition is CGO:LSTN=80:20 which is matched quite well by the effective composition CGO:LSTN=22:78 of the characterized sample volume. The structure has a cube-size of 384^3 voxels. This sample shows some inhomogeneities. However, this problem cannot be resolved e.g., by cropping the sample and will need to be accounted for in the discussion of the data. Thus, the full structure without cropping is used for the determination of the microstructure properties described in section 3.1.1 of the main article. A selection of microstructure properties for this structure is also reported in table 14 in the main article.

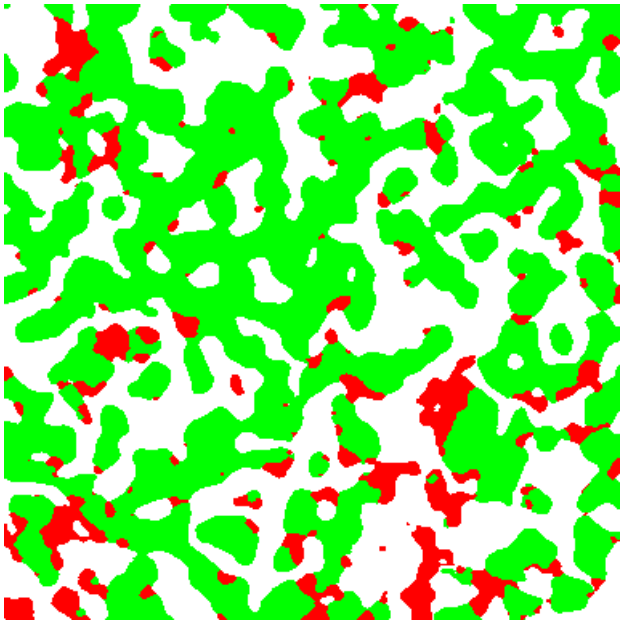

(a) Tomography, central slice in the XZ-plane.

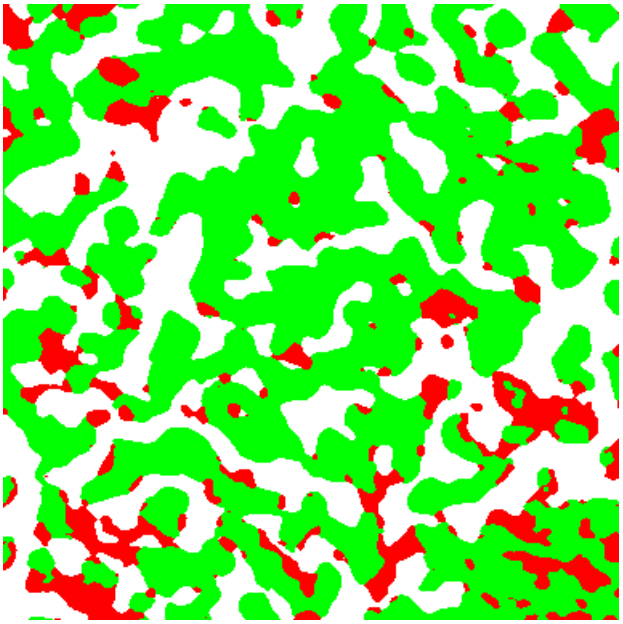

(b) Tomography, central slice in the YZ-plane.

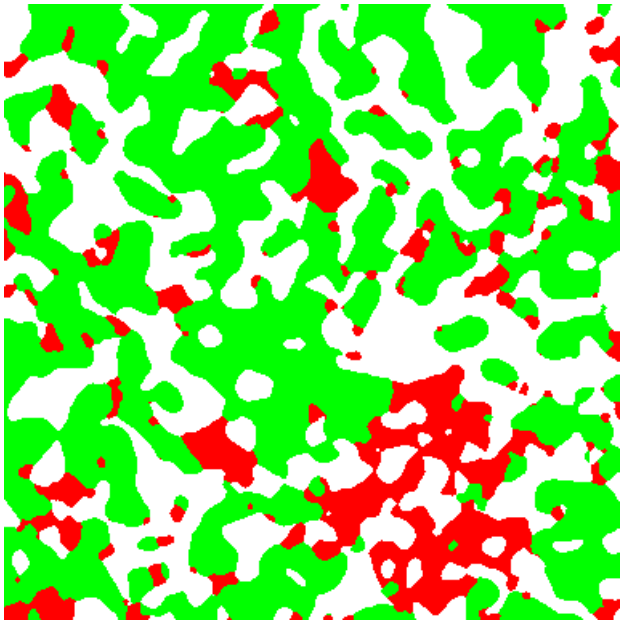

(c) Tomography, central slice in the XY-plane.

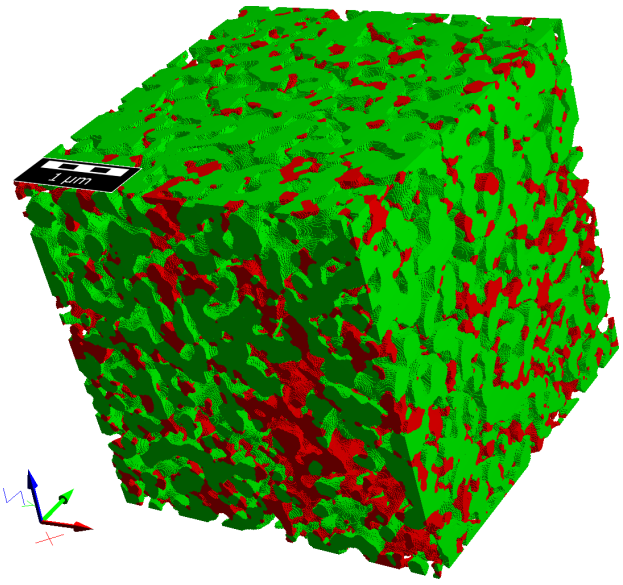

(d) Tomography, 3D structure.

Fig. 12 Original CGO80-LSTN20 tomography structure: central orthoslices a)-c) and 3D-view d). Colour code: green = CGO, red = LSTN, white/transparent = pore. The sample volume is a cube with a side length of 3.84 µm.

H Example for a standardized characterization of virtual three-phase structures from sphere-packing

In Fig. 13 a), the covariance functions are reported for the different phases and samples of the virtual sphere-packing dataset. Due to the well-defined geometries of the sphere-packing structures, the shape of the covariance functions is very steady and does not show additional curvatures like for the LSTN-CGO dataset (Fig. 12 a) in the main article).

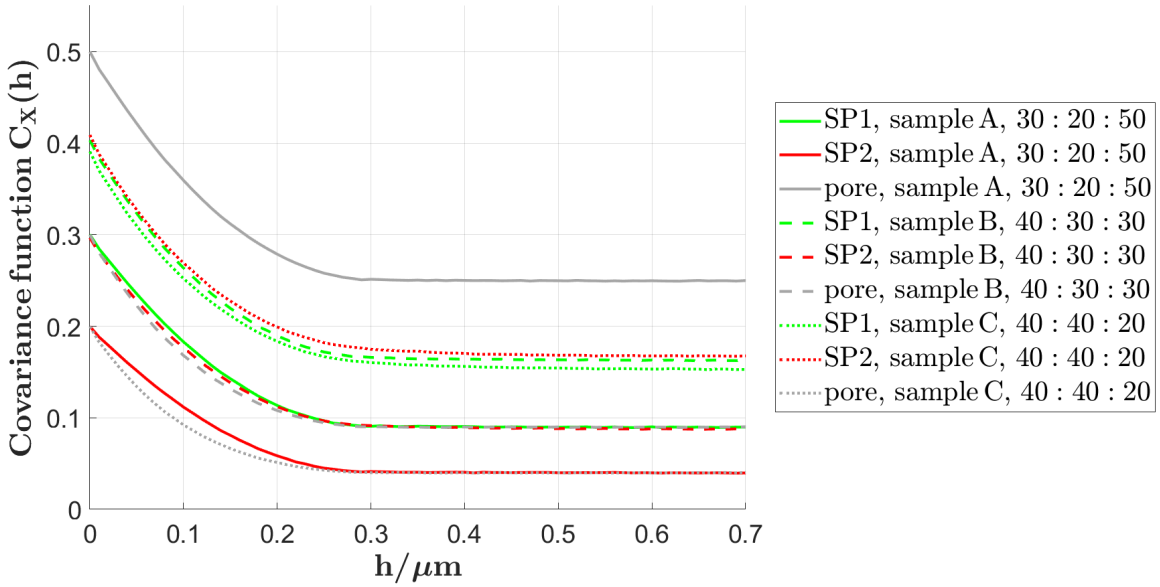

Fig. 13 Covariance functions of SP1, SP2 and the pore-phase for the virtual sphere-packing structures.

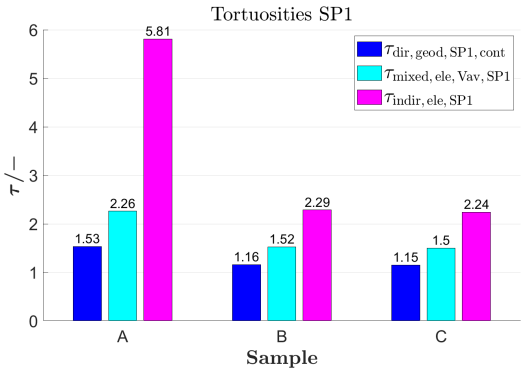

(a) SP1.

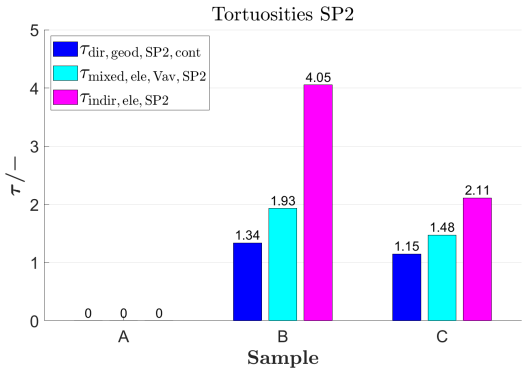

(b) SP2.

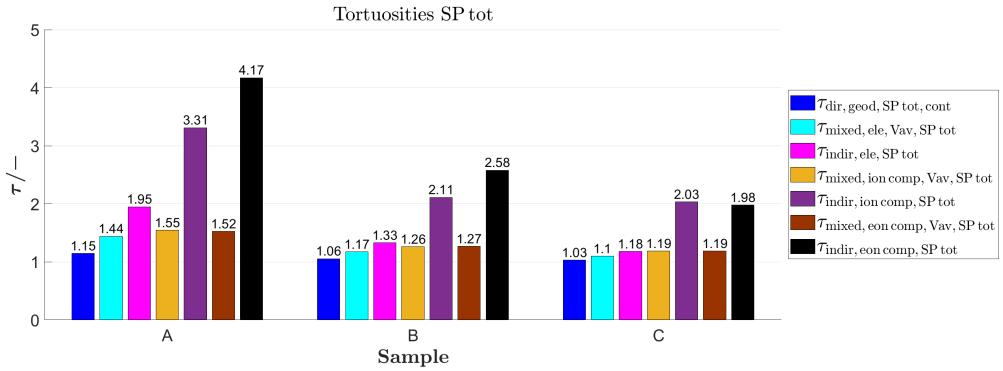

(c) Total solid phase (SP tot).

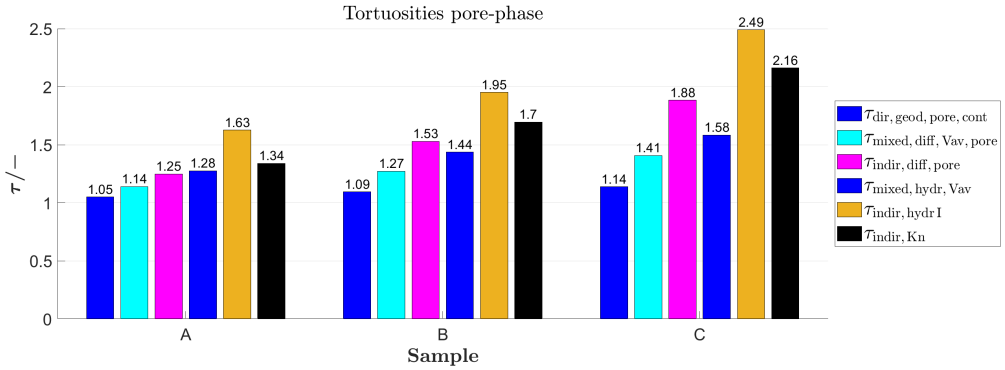

(d) Pore-phase.

Fig. 14 Different tortuosities for a) SP1, b) SP2, c) total solid-phase (SP tot) and d) the pore-phase for the virtual sphere-packing structures. The used variables are summarized in the tables 6-8 in the main article.

The full set of the characterized tortuosities for the sphere-packing dataset is reported in Fig. 14. Thereby, the relations between the different tortuosities discussed in section 3.1.1 in the main article for the LSTN-CGO dataset (Fig. 14 in the main article) are confirmed. The indirect physics-based tortuosities are generally larger than the direct geometric based geodesic tortousities for the same transporting phase. The mixed volume averaged tortuosities are in-between.

In Fig. 15, the M-factors for prediction II are reported together with the simulated M-factors for the two solid phases, the total solid phase and the pore-phase for the virtual sphere-packing structures. Moreover, the two terms for the M-factor prediction II from phase volume fraction / constrictivity term and the tortuosity term are reported along. The results with prediction II are very similar to the results of prediction I reported in Fig. 15 in the main article.

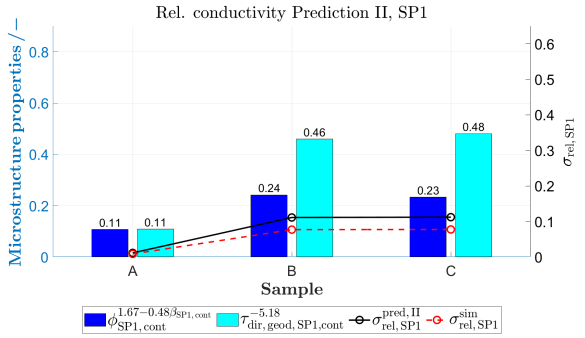

(a) SP1.

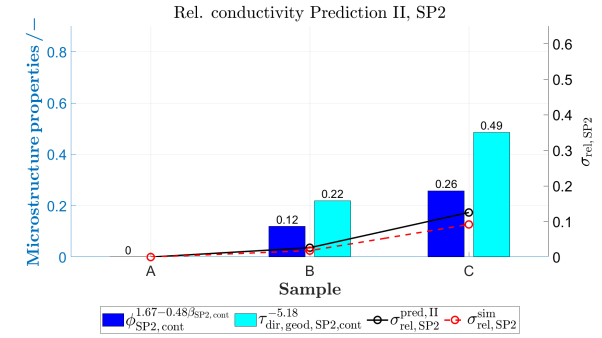

(b) SP2.

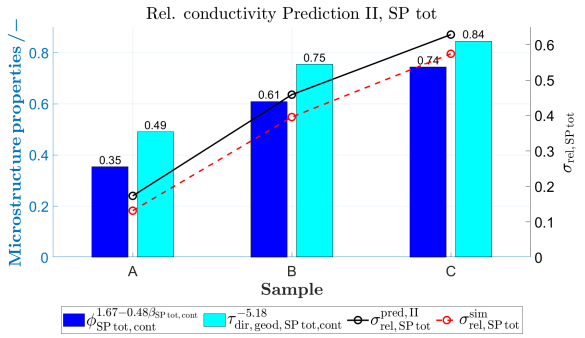

(c) Total solid phase (SP tot).

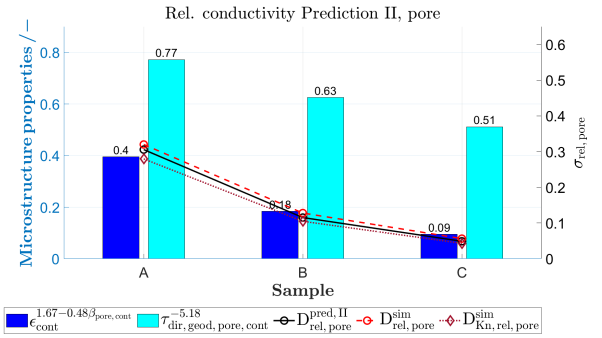

(d) Pore-phase.

Fig. 15 M-factor prediction II (black line) and its two components (volume fraction and constrictivity effect $\phi^{1.67-0.48\beta}$ and tortuosity effect $\tau_{\mathrm{dir,geod}}{}^{-5.18}$) and simulated M-factors (red lines), for a) SP1, b) SP2, c) total solid-phase (SP tot) and d) the pore-phase of the sphere-packing structures. The used variables are summarized in the tables 10 and 9 in the main article.

In Fig. 16 b), the simulated gas permeability of the pore-phase is plotted together with the two predictions for the permeability reported in table 12 in the main article. The agreement between predictions and simulation is rather poor. Nevertheless, the predictions correctly catch the trends and are thus helpful to interpret the microstructure limitations affecting permeability. The hydraulic radius (Fig. 16 a)) decrease significantly for decreasing porosity. Together with the direct effect of the porosity and the tortuosity, this results in a tremendous decrease of the permeability (Fig. 16 b)) for decreasing porosity.

The characteristic Knudsen radius, which is a result of the Knudsen transport simulation (see section 2.3.3.2 in the main article), is also reported in Fig. 16 a). It is quite similar to the hydraulic radius $r_{\mathrm{hc\,II,\,pore,\,cont}}$ defined in Eq. 28 in the main article.

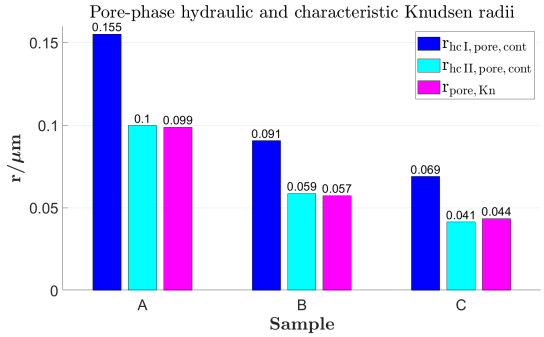

(a) Pore-phase, hydraulic and Knudsen radii.

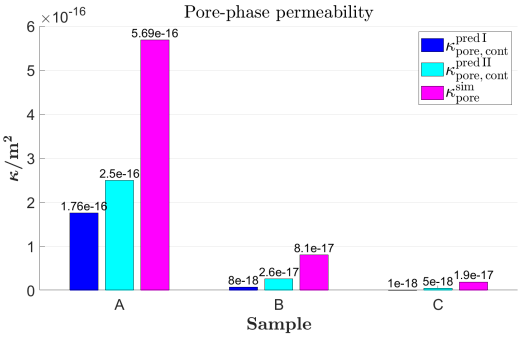

(b) Pore-phase, gas permeability

Fig. 16 Additional characteristics of the pore-phase: a) hydraulic and Knudsen radii and b) gas permeability (predicted and simulated). The used variables are summarized in the tables 12 and 13 in the main article.

References

1 P. Marmet, L. Holzer, T. Hocker, G. Boiger, J. Hilden, S. Reeb and M. Fingerle, GeoDict User Meeting 2021, 2021, p. 22.

2 H. Moussaoui, J. Laurencin, Y. Gavet, G. Delette, M. Hubert, P. Cloetens, T. Le Bihan and J. Debayle, *Computational Materials Science*, 2018, **143**, 262–276.

3 *GeoDict simulation software Release 2022, by Math2Market GmbH, Germany, doi.org/10.30423/release.geodict2022*.

4 L. Holzer, P. Marmet, M. Fingerle, A. Wiegmann, M. Neumann and V. Schmidt, *Tortuosity and microstructure effects in porous media: classical theories, empirical data and modern methods*, Springer Cham, 1st edn, 2023.

5 T. Nakamura, K. Yashiro, A. Kaimai, T. Otake, K. Sato, T. Kawada and J. Mizusaki, *Journal of The Electrochemical Society*, 2008, **155**, B1244–B1250.

6 C. Graves, L. Martinez and B. R. Sudireddy, *ECS Transactions*, 2016, **72**, 183–192.

7 A. Nenning, M. Holzmann, J. Fleig and A. K. Opitz, *Materials Advances*, 2021, **2**, 5422–5431.

8 A. Sciazko, Y. Komatsu, R. Yokoi, T. Shimura and N. Shikazono, *Journal of the European Ceramic Society*, 2022, **42**, 1556–1567.

9 A. Heel, D. Burnat and L. Holzer, *NRP70, Energy Turnaround*, 2023, `https://www.nfp-energie.ch/en/projects/977/`.

10 D. Burnat, R. Kontic, L. Holzer, P. Steiger, D. Ferri and A. Heel, *Journal of Materials Chemistry A*, 2016, **4**, 11939–11948.

11 E. Castillo-Martínez, A. Durán and M. Á. Alario-Franco, *Journal of Solid State Chemistry*, 2008, **181**, 895–904.

12 B. C. Steele, *Solid State Ionics*, 2000, **129**, 95–110.

13 D. Burnat, G. Nasdaurk, L. Holzer, M. Kopecki and A. Heel, *Journal of Power Sources*, 2018, **385**, 62–75.

14 X. Zhou, N. Yan, K. T. Chuang and J. Luo, *RSC Advances*, 2014, **4**, 118–131.

15 M. D. Uchic, L. Holzer, B. J. Inkson, E. L. Principe and P. Munroe, *MRS Bulletin*, 2007, **32**, 408–416.

16 L. Holzer and M. Cantoni, *Nanofabrication Using Focused Ion and Electron Beams: Principles and Applications*, Oxford University Press, 2011.

17 M. Cantoni and L. Holzer, *MRS Bulletin*, 2014, **39**, 354–360.